coatings

MDPI

Article

Corrosion Protection of C90300 Bronze by Diamond-like Carbon Coatings: Suppression of Cathodic Oxygen Reduction

Lázaro Aleixo dos Santos [1,2,3,*], Henri Stephan Schrekker [4], Silvia Margonei Mesquita Tamborim [1], Vladimir Jesus Trava-Airoldi [5] and Luís Frederico Pinheiro Dick [2]

[1] Department of Physical Chemistry, Institute of Chemistry, Federal University of Rio Grande do Sul (UFRGS), Av. Bento Gonçalves 9500, Porto Alegre 91501-970, RS, Brazil; silviatamborim@gmail.com
[2] Electrochemical Processes and Corrosion Laboratory, Federal University of Rio Grande do Sul (UFRGS), Av. Bento Gonçalves 9500, Porto Alegre 91501-970, RS, Brazil; lfdick@ufrgs.br
[3] Metallurgical and Materials Engineering Department, Polytechnic School, University of São Paulo (USP), São Paulo 05508-030, SP, Brazil
[4] Laboratory of Technological Processes and Catalysis, Institute of Chemistry, Federal University of Rio Grande do Sul (UFRGS), Av. Bento Gonçalves 9500, Porto Alegre 91501-970, RS, Brazil; schrekker@iq.ufrgs.br
[5] National Institute for Space Research (INPE), Av. dos Astronautas 1758, São José dos Campos 12227-010, SP, Brazil; vladimir.airoldi@inpe.br
* Correspondence: aleixolazaro@gmail.com; Tel.: +55-51-98439-7692

Highlights

What are the main findings?

- The DLC/a-Si:H coating on C90300 bronze yielded a 97% initial corrosion protection efficiency.
- The coated bronze showed polarization resistance up to 122 times higher than the bare alloy.
- Mott–Schottky analysis suggested distinct semiconducting contributions within the DLC/a-Si:H system.
- Reduced cathodic activity may involve physical barrier effects and restricted interfacial electron transfer.
- DLC stabilizes friction, but wear resistance is limited due to delamination mechanisms.

What are the implications of the main findings?

- The DLC film acts as a robust physical barrier in aggressive chloride-rich environments.
- The coating suppresses cathodic electrochemical activity, potentially through combined barrier effects and restricted interfacial electron transfer.
- Both anodic dissolution and cathodic reaction rates on the bronze surface are largely reduced.

Check for updates

Academic Editor: Peter Rodič

Received: 20 August 2026
Revised: 6 September 2026
Accepted: 28 October 2026
Published: 3 November 2026

Copyright: © 2026 by the authors. Licensee MDPI, Basel, Switzerland. This article is an open access article distributed under the terms and conditions of the Creative Commons Attribution (CC BY) license.

Abstract

This study investigates the corrosion protection of amorphous hydrogenated diamond-like carbon (DLC) films over C90300 bronze alloy (Cu-Sn-Zn) in chloride-rich environments. To overcome poor adhesion between copper and carbon, we used an amorphous hydrogenated silicon (a-Si:H) interlayer via modified pulsed DC PECVD. Raman spectroscopy and spectroscopic ellipsometry characterized the DLC layer, revealing a thickness of approximately 177 nm and an estimated hydrogen content of 35.2 at%. Electrochemical evaluation in a 3.5% NaCl solution over 30 days showed that the DLC coating provides a strong barrier effect, achieving an initial protection efficiency of 97% and polarization resistance (Rp) up to 122 times higher than the bare alloy. Cathodic polarization measurements demonstrated reduced cathodic current densities for the DLC-coated bronze, consistent with suppression

of oxygen reduction under aerated conditions. Mott–Schottky analysis suggested that the electronic properties of the multilayer coating may contribute to restricted interfacial electron transfer, in addition to its physical barrier effect. Tribological tests indicated that the DLC coating reduced and stabilized the coefficient of friction (~0.50), although the coated system exhibited more extensive wear-track damage, potentially involving coating rupture, material transfer, and third-body abrasion. These findings demonstrate the potential of DLC coatings to enhance the corrosion resistance of bronze, although the progressive decrease in electrochemical protection during prolonged immersion highlights the need for further optimization of coating durability.

Keywords: DLC coatings; bronze; corrosion protection; oxygen reduction reaction; electrochemical impedance; Mott–Schottky

1. Introduction

High-tin bronzes, such as C90300, have special properties, including high corrosion resistance in chlorides and low friction, and therefore have a wide range of applications, such as electrical wiring, heat exchange, coinage, weapon production, statues, and ornaments [1,2]. This versatility stems from their high ductility, hardness, low melting point, high corrosion resistance, and non-magnetic properties [1–3]. Copper-tin alloys, commonly known as bronze, can also contain zinc (Zn), lead (Pb), and phosphorus (P) [2,4–8]. Bronze alloy composition matters because different elements impart different characteristics, such as metal and patina color, alloy value, and casting method [8]. For example, Tin (Sn) increases hardness; 4%–10% tin increases wear resistance and hardness, while Pb improves pourability [7]. Copper alloys with 4%–8% tin produce bronzes that are not only highly corrosion-resistant but also aesthetically appealing, making them particularly valuable in cultural heritage [8–10].

Bronze alloys are widely used in tribological systems because they combine low friction coefficients with high wear resistance, especially in sliding contacts under severe mechanical conditions. Their tribological performance depends on alloy composition and microstructure: graphite or lead phases reduce friction by promoting lubricating transfer films, while Sn and Ni improve hardness, strength, and wear resistance [11,12]. In Cu–Sn bronze coatings, balancing hardness and toughness minimizes counterface wear and reduces the risk of coating delamination, making bronze particularly suitable for friction pairs such as bearings, pistons, and hydraulic pump components [13].

When exposed to the natural environment, metallic substrates gradually degrade, forming layers of corrosion products with distinct compositions and structures [14]. In bronze-based artifacts, these corrosion products are known as patina [15,16]. Natural patinas typically form on artifacts exposed to the atmosphere, water, seawater, or soil for extended periods [17]. Pollution (smoke, particulate matter, acid rain), bird excrement, other living organisms, thermal shock, and vandalism can also significantly contribute to the degradation of bronze structures [9]. Patina chemical compositions are diverse, but they generally consist of copper oxides (cuprite—Cu_2O ruby red; tenorite—CuO black), carbonates (malachite—$Cu_2CO_3(OH)_2$ green), hydroxychlorides and chlorides (atacamite and paratacamite—$Cu_2(OH)_3Cl$ dark green, nantokite—CuCl green), sulfates and sulfides (brochantite—$Cu_4SO_4(OH)_6$ emerald green or black, antlerite—$Cu_3(SO_4)(OH)_4$ green, chalcocite—Cu_2S gray) [9,13,14]. However, certain conditions can destabilize the patina, accelerating bronze corrosion and degradation, and causing irreversible damage [16–20]. The interaction between copper, chloride, moisture, and oxygen in the air drives a cyclic

degradation process known as bronze disease [10,14,20]. The corrosion products are mostly basic copper chlorides, which are powdery, voluminous, and prone to crumbling on the surface. These corrosion products can disfigure the object, and light exposure can accelerate the process [16,20]. Chloride ions react with copper to form nantokite (CuCl) on the metal surface. When nantokite contacts moisture and oxygen, it reacts to form the bulky, porous, powdery atacamite (or paratacamite—$Cu_2(OH)_3Cl$). This reaction causes surface cracks due to volume changes, allowing chlorides and water to penetrate the corrosion-product layer and eventually reach the metal surface [21].

Researchers have extensively studied dealloying in binary model alloys. The Erlebacher model [22] describes how selective dissolution of the less noble species, along with concurrent surface diffusion of the remaining species, leads to a bicontinuous porous structure. However, bronze corrosion is more complex because two or more less noble elements may dissolve simultaneously or sequentially.

Selective dissolution of less noble elements, such as Zn and Sn, may lead to Cu enrichment at the alloy surface [23–25]. Under aerated conditions, Cu-rich regions can support the oxygen reduction reaction (ORR), potentially increasing local cathodic activity and influencing corrosion kinetics [26]. Moreover, the selective removal of alloying elements may generate voids and a porous, sponge-like structure [22], increasing the electrochemically accessible surface area and potentially facilitating cathodic reactions.

Song and Tegus [24] investigated the corrosion behavior of bronze alloys in chloride media and found that in Cu–Sn bronzes, the Cu-rich α phase is preferentially attacked. In contrast, the Sn-rich δ phase forms a protective SnO_2 layer that improves corrosion resistance. Chloride ions promote selective dissolution of copper, destabilize passive films, and form CuCl and Cu_2O, ultimately accelerating localized dealloying.

Zhang et al. [25] examined bronze corrosion in atmospheric environments relevant to cultural heritage, emphasizing that ancient Cu–Sn–Pb bronzes develop complex corrosion layers composed of protective oxides (Cu_2O, $Cu_2(OH)_2CO_3$, SnO_2) and harmful chlorides such as $Cu_2(OH)_3Cl$. The microstructural heterogeneity of these alloys, combined with environmental fluctuations in humidity and chloride exposure, drives selective and intergranular corrosion.

High Zn contents significantly increase copper alloys' susceptibility to selective dissolution. As Sharifi and Ranjbar [23] show, brasses with more than 15 wt.% Zn, especially dual-phase α + β alloys, are highly prone to dezincification because Zn leaches preferentially, leaving a porous Cu-rich matrix. This process accelerates in chloride-rich, oxygenated environments, where the protective Cu_2O film breaks down and cuprous chlorides form, enhancing localized attack. Tin additions, by contrast, may mitigate dezincification by promoting passivation and stabilizing the oxide layer, though their effect depends on alloy microstructure and environmental aggressiveness. Overall, corrosion and dealloying in Cu-based alloys such as brasses and bronzes are governed by the complex interplay between alloy composition, phase structure, and environmental factors that determine the kinetics of selective dissolution and the evolution of localized corrosion damage.

To enhance corrosion resistance, protective films can be applied to metals to serve as a barrier between the substrate and the aggressive environment. In this context, applying a diamond-like carbon (DLC) film is particularly advantageous because it resists both mechanical wear and corrosion [27] without altering heat transfer across the interfaces.

DLC is a metastable class of carbon-based materials formed by amorphous carbon with significant fractions of sp^3-sp^3 and sp^2-sp^2 carbon (C-C, C=C) bonds and hydrogenated carbons (C-H) [28,29]. This material is a semiconductor and exhibits high mechanical hardness, chemical inertness, optical transparency, a low coefficient of friction, and biocompatibility [14,27–30]. Its properties depend on the film's chemical composition, the

sp^3/sp^2 bond ratio, and hydrogen content [31,32]. The deposition technique, precursor gas, and incorporation of metals or nanoparticles affect DLC films' chemical composition and mechanical properties [27].

Regarding anti-corrosion performance, DLC and amorphous carbon improve corrosion protection in chloride [29] and even in the human body environment, improving cell adhesion and supporting their use in coated dental implants [33]. DLC films, with or without modifications (multilayered or doped), over AISI 4340 steel also improve corrosion resistance in chloride media [27,34].

Due to a low density of chemical bonds at the DLC-metal surface interface and very high total compressive stress on these coatings, DLC often has relatively low adhesion to the metallic substrate [30]. The low affinity between Cu and C challenges carbon film deposition. However, silicon forms sufficiently strong carbide bonds and exhibits high mutual diffusion with copper; together with high C diffusion in silicon, an a-Si:H interlayer provides an interaction between Cu (principal alloy element of bronze) and C from DLC, reducing the residual stress in DLC films and improving adhesion [27].

This research project aims to deposit DLC coatings on C90300 bronze substrates to enhance corrosion resistance without compromising bronze's tribological properties. The project also seeks to evaluate how DLC influences key electrochemical processes, particularly the kinetics of the cathodic reaction and oxygen reduction on bronze surfaces. By understanding how DLC films affect these reactions and the coating's overall protective behavior, the study aims to establish DLC-coated bronze as a high-performance material for demanding operating conditions.

2. Materials and Methods

Bronze C90300 samples provided by Ferramentas Gerais Comércio e Importação de Ferramentas e Máquinas LTDA (Porto Alegre, Brazil), with nominal composition of 86 wt% Cu, 9 wt% Sn, and 5 wt% Zn, were cut into Ø = 1 cm discs, sanded with SiC sandpapers of 200 to 2000 #, and finally mirror-polished using 0.05 µm alumina polishing suspension. After polishing, the alloy disks were cleaned with acetone and isopropyl alcohol. Researchers grew amorphous hydrogenated silicon (a-Si:H) interlayers using a modified pulsed-DC PECVD system [27]. Researchers at the Instituto Nacional de Pesquisas Espaciais (INPE) in Brazil developed this modified deposition technique and used it to deposit both a-Si:H and DLC. The coating process used Ar and Ar + H_2 plasmas to remove surface impurities, Ar + SiH_4 plasma to deposit the a-Si:H layer, and Ar + acetylene plasma to deposit DLC. Table 1 summarizes the deposition conditions.

Table 1. Experimental conditions used in the deposition of a-Si:H and DLC.

Duration/s	Applied Voltage/V	Pressure/10^{-6} bar	
1800	–600	3.2	Cleaning Ar
3600	–800	4.7	Ar + H_2
180	–1200	3.2	Ar + SiH_4
60	–800	3.7	Ar + SiH_4 + C_2H_2
1500	–800	3.5	Ar + C_2H_2

The thickness of the DLC film was measured by Ellipsometry using SOPRA GES-5E equipment (Japan). Spectroscopic data were acquired over 500–700 nm by fitting the α and β parameters with the analyzer fixed at 45°. The angle of incidence was set to 75.11°.

Electrochemical experiments were performed in a three-electrode cell using an AUTOLAB apparatus model µ AUTOLAB/FRA 2 for EIS; an Autolab PGSTAT302N was used for linear sweep voltammetry and EIS for Mott–Schottky measurements (Metrohm Autolab,

Utrecht, The Netherlands). The bronze C90300 discs with an exposed window of 0.78 cm^2 were used as the working electrode in a 3.5% NaCl solution (~0.6 mol L^{-1}). A platinum gauze and a saturated calomel electrode (SCE) were used as auxiliary and reference electrodes, respectively. Electrochemical experiments, including cathodic and anodic linear sweep voltammetry, were initiated 1 h after open-circuit potential stabilization. EIS was performed at open-circuit potential, over the frequency range of 100 kHz to 10 mHz, with 10 points per decade and an ac voltage amplitude of 10 mV. To assess the time-stability of the DLC film on bronze, EIS experiments were performed at different immersion times up to 30 days. We fitted the impedance data using Nova 2.0 software (Metrohm Autolab, Utrecht, The Netherlands).

Electrochemical impedance spectroscopy for Mott–Schottky measurements was obtained in a 0.01 mol L^{-1} $Na_2B_4O_7$ and 0.0125 mol L^{-1} H_3BO_4 solution at 25 °C using a standard three-electrode cell under anaerobic conditions. Results are reported with respect to the standard hydrogen electrode (SHE). The frequency range of the space-charge layer was determined from impedance spectra measurements at the potentials E of −500, −250, 0, +250, and +500 mV (SHE). Mott–Schottky plots were obtained in the potential range of −400 to 400 mV (SHE) at 1 and 100 Hz, which were inferred from the applied potential E dependence of the real part of the capacitance C′, as described in the literature [35]. To avoid electron–hole injection into the electrode due to the O_2 reduction reaction, the cell was purged with high-purity N_2 for 2 h before the electrochemical measurements. Local ionic current density maps (i maps) of DLC-coated C90300 bronze were acquired in 0.01 mol L^{-1} NaCl solution using an Applicable Electronics SVET system operating under OCP conditions. The scanning microelectrode was made of Pt/Ir wire, with a tip diameter of 10 μm, vibrating with an amplitude of ±5 μm scanned at 50 μm from the sample surface. An area of 0.559 × 0.330 mm was scanned. Measurements were performed at room temperature. The acquired signals were processed using Aset 2.0 software to generate local ionic current density maps. A diluted NaCl solution was selected to reduce electrolyte conductivity, thereby increasing the potential gradients associated with local ionic currents. SVET measurements were performed exclusively on DLC-coated bronze to investigate localized electrochemical activity, whereas comparisons with uncoated bronze were conducted using polarization and EIS measurements.

The samples were characterized using a Tescan VEGA3 scanning electron microscope (SEM - TESCAN, Brno, Czech Republic) equipped with an Oxford X-ACT energy-dispersive spectrometer (EDS- Oxford Instruments NanoAnalysis, High Wycombe, UK) and a field-emission gun scanning electron microscope (SEM-FEG - Carl Zeiss Microscopy GmbH, Jena, Germany) Zeiss Auriga.

Raman spectroscopy was performed to characterize the DLC film using an argon laser at 514 nm. The equipment used was an RLabRam HR Evolution Raman Spectrometer (Horiba Scientific France SAS, Villeneuve-d'Ascq, France), and the obtained spectra were analyzed using the software Fityk 1.3.1.

Reciprocating tribological tests were performed using a UMT tribometer (Bruker Nano, Santa Barbara, CA, USA) under dry sliding conditions. A 10 mm diameter SAE 52100 chrome steel ball was used as the counterbody. The tests used a 5 mm stroke length, 0.28 Hz frequency, and a 10 N normal load for 30 min. In load-step experiments, the normal load was increased from 0 N to 10 N after 30 s. The coefficient of friction (COF) was continuously recorded throughout the test. Bruker Contour GT-K optical interferometer (Bruker Nano, Inc., Tucson, AZ, USA) was used to acquire images of the surface topography. The tribological experiments were carried out at the Surface Phenomena Laboratory (LFS), part of the Polytechnic School of the University of São Paulo. All experiments were performed at least in triplicate to ensure reproducibility.

3. Results and Discussion

3.1. DLC Characterizations

3.1.1. Ellipsometry

Spectroscopic ellipsometry measurements were carried out at an incidence angle of 75.11°, with the analyzer fixed at 45°, and the data were fitted to the α and β parameters. The spectral regression range extended from 0.50 to 0.70 µm, using a microspot aperture set to 0. The fit was evaluated using the standard deviation ($\sigma = 7.47 \times 10^{-4}$) and the coefficient of determination ($R^2 = 0.9769$), indicating excellent agreement between the experimental and calculated data. The measured refractive index of the DLC film set was 1.702 ± 0.0775; the analysis revealed a thickness of approximately 176.634 ± 0.785 nm. The measured film thickness of approximately 177 nm indicates a well-defined, uniform coating within the analyzed region, suggesting reasonable deposition control. The refractive index *n* decreases slightly with increasing wavelength, from 1.784 at 500 nm to 1.598 at 700 nm, a behavior typical of dielectric or semiconducting materials exhibiting normal dispersion.

3.1.2. Raman Spectroscopy

Figure 1 shows a typical Raman spectrum for DLC films deposited on bronze C90300 with an amorphous hydrogenated silicon interlayer (a-Si:H), hereafter referred to as C90300/a-Si:H/DLC. The spectrum shows a single, asymmetric peak between 1000 and 1700 cm^{-1}, which was deconvoluted and fitted with the Fityk code using two Gaussian functions. The D-band, centered around 1350 cm^{-1}, relates to aromatic ring deformations in disordered graphite phases, and the G-band, centered around 1550 cm^{-1}, relates to sp^2-hybridization stretching in carbon chains and rings.

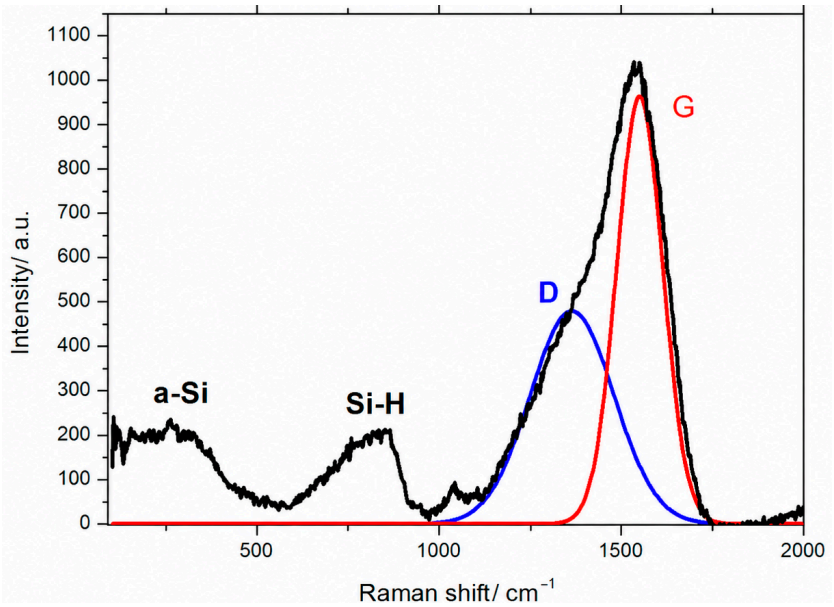


Figure 1. Raman spectrum of the DLC coating deposited on C90300 bronze with an a-Si:H interlayer, showing the characteristic D and G bands of amorphous carbon.

The degree of hydrogenation of the DLC film can be determined as the atomic percentage of hydrogen H at% by Equation (1) [34]:

$$H[at\%] = 21.7 + 16.6log\left(\frac{m}{I(G)}\right) \quad (1)$$

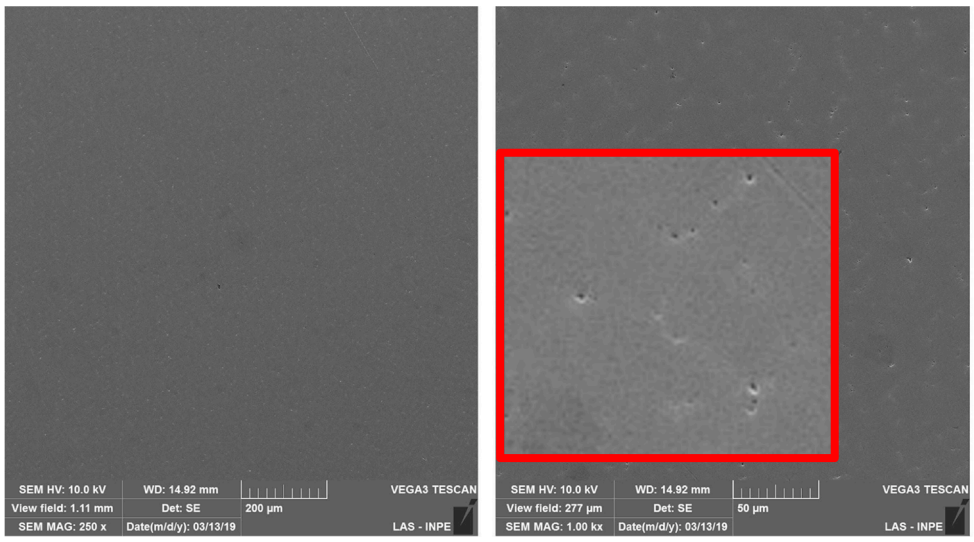
where I(G) and I(D) are the G and D peak intensities and m is the slope of the spectrum between 1000 and 1800 cm^{-1}. The I(D)/I(G) ratio of 0.499 and the broad G-band full width

at half maximum (FWHM) of approximately 130 cm^{-1} are consistent with a disordered amorphous carbon network containing sp^2-bonded carbon clusters. Based on the empirical Raman relationship described in Equation (1) [34], the hydrogen content was estimated to be 35.2 at%. This value, together with the observed spectral characteristics, is consistent with the formation of a hydrogenated amorphous carbon (a-C) film. However, because the hydrogen content was inferred indirectly from an empirical relationship, the estimate is subject to uncertainties related to the carbon network structure and measurement conditions and should not be interpreted as a direct determination of hydrogen concentration. Besides the DLC characteristic bands, the Raman spectrum in Figure 1 shows at wave numbers below 1000 cm^{-1}, two bands related to the a-Si:H interlayer: The first can be assigned to the amorphous silicon structure, and the second one to the silicon–hydrogen bonds.

3.1.3. Film Morphology SEM-EDS

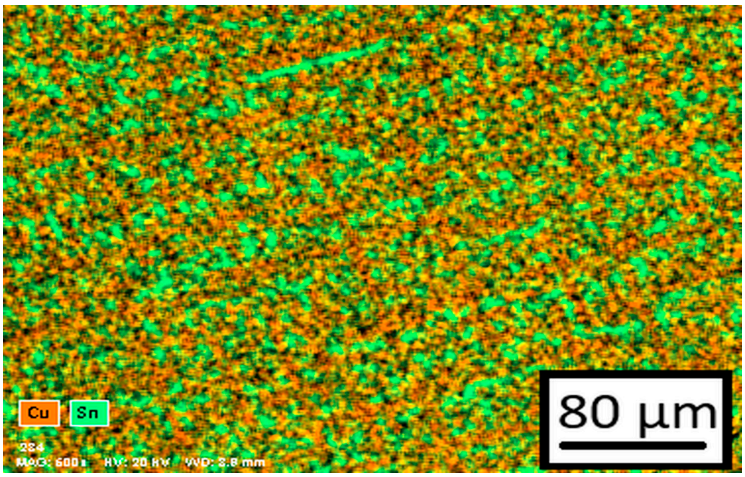
Top-surface SEM images of polished bronze C90300 before (Figure 2) and after DLC deposition (Figure 3) confirm that the samples showed no signs of exfoliation before the immersion test and had smooth surfaces. The corresponding EDS images show no significant surface segregation of Sn, as reported for Cu_4Sn and Cu_6Sn [31]. In fact, Cu and Sn were well distributed at the surface, consistent with the formation of a Cu/Sn solid solution [3].

Figure 3 shows the surface morphology of the deposited DLC film, revealing a relatively homogeneous coating characterized by small surface features and dispersed microstructural irregularities typical of amorphous carbon layers. Multiple regions were selected for EDX analysis, indicated by the labeled spectra boxes, allowing assessment of the film's elemental composition. The EDX results confirm that the surface is predominantly carbon (58.4 at%), consistent with a DLC coating, with significant silicon (25.5 at%) likely originating from the deposition process or interlayer. Smaller amounts of copper (13.8 at%) and traces of tin and oxygen suggest partial substrate contribution and/or surface contamination.

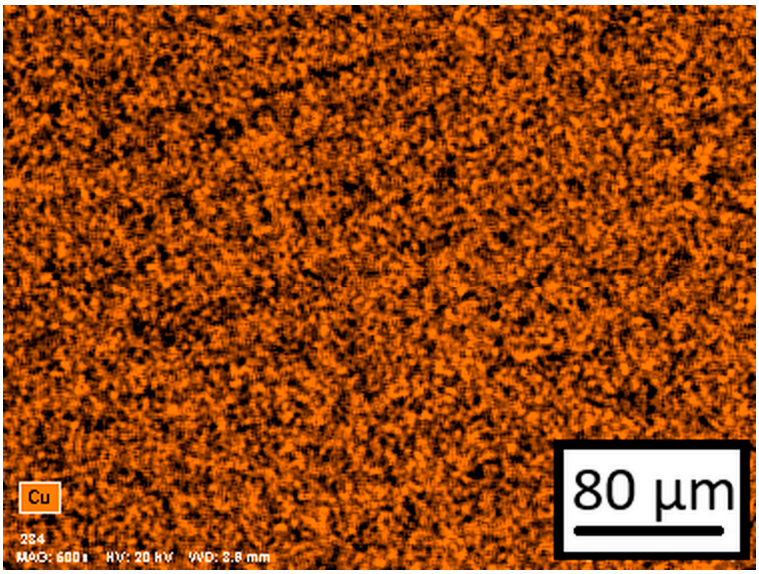


(**a**) (**b**)

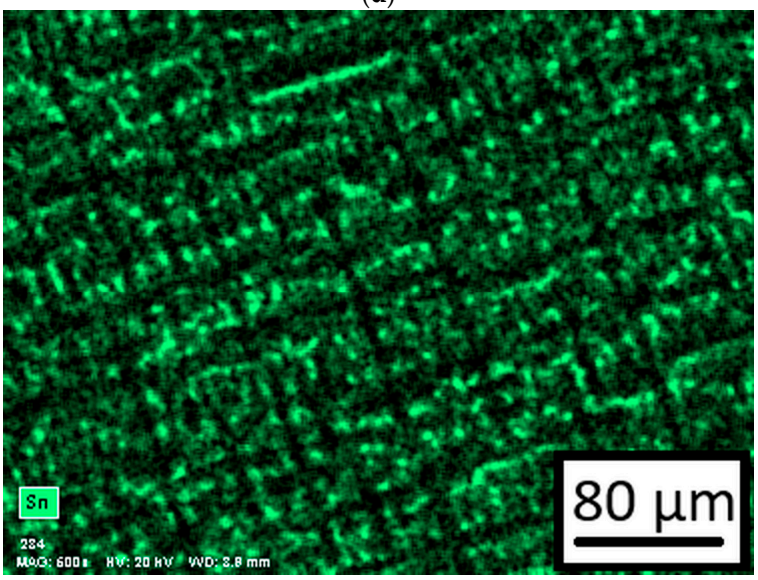
Figure 2. *Cont.*



(**c**)

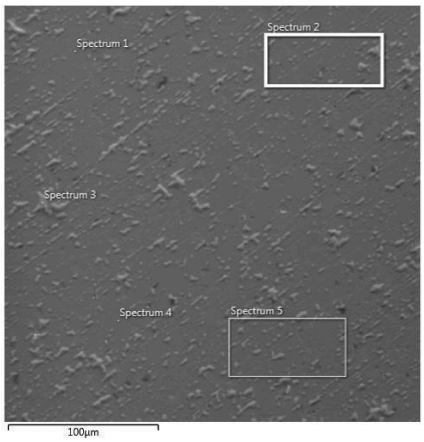


(**d**)



(**e**)

Figure 2. SEM images of C90300 bronze alloy after polishing: (**a**) 250×; (**b**) 1000×; (**c**–**e**) EDX maps of the surface.



Element	at%	σ
Cu	13.8	0.2
Si	25.5	0.2
C	58.4	0.3
Sn	0.4	0.2
O	1.9	0.1

Figure 3. SEM images of the DLC film and surface EDX.

3.2. Electrochemical Experiments

3.2.1. Open Circuit Potential Measurements

Open circuit potential (OCP) measurements were carried out over 30 days in 3.5% NaCl aqueous solution to obtain initial electrochemical activity information that occurred at the electrode/solution interface. Both the electrolyte and concentration were chosen based on previous studies about chloride corrosion of bronze or copper [5,22,36–39]. Figure 4 shows the OCP evolution for two electrodes, bronze C90300 with and without DLC film. For bronze C90300, the OCP values agree with those reported. Throughout the period evaluated, regardless of DLC film presence, the initial OCP values were more negative and shifted toward less negative values until stabilization. The initial increase may relate to passive film formation on the bronze surface [5]. Over time, further passive-film growth stabilized the OCP. The OCP values for bronze coated with DLC are less negative than those for uncoated bronze C90300. This finding indicates that the C90300/a-Si:H/DLC coating protected the bronze alloy in a chloride environment for 30 days [40].

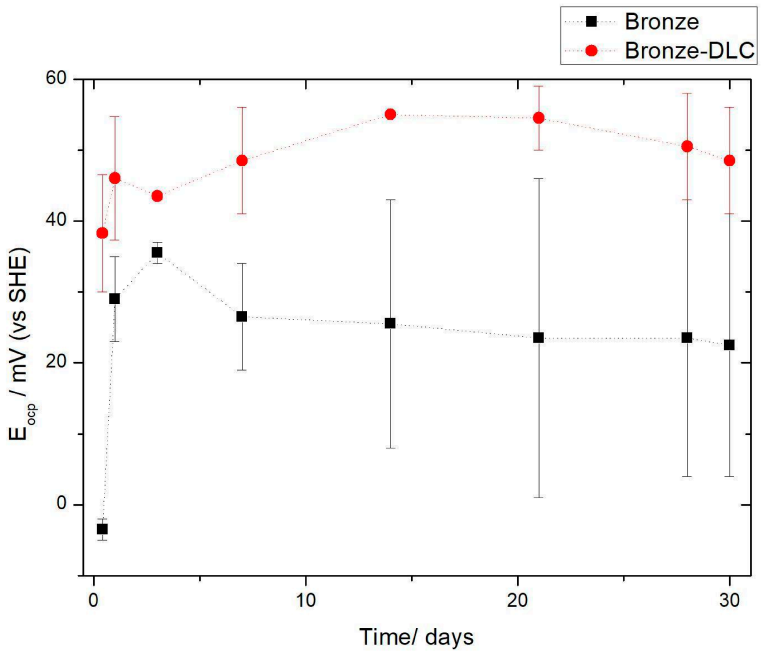


Figure 4. Open-circuit potential time curves for uncoated C90300 (■) and C90300/a-Si:H/DLC (●) in 3.5% NaCl aqueous solution.

3.2.2. Linear Sweep Voltammetry

Polarization curves after 1 h of immersion in an aqueous 3.5% NaCl solution are shown in a semilogarithmic diagram of overpotential relative to the corrosion potential ($\Pi = E_{applied} - E_{corr}$) versus current density j (Figure 5). Anode polarization corresponds to copper oxidation and, for the bare alloy, is controlled by diffusion of soluble copper chlorides and copper electrodissolution, resulting in a monotonic increase in current. For the C90300/a-Si:H/DLC system, the maximum current occurred at 2 V, with lower anodic current densities and a shallower slope. This polarization confirms that the DLC coating increased bronze corrosion resistance. Comparing both systems shows differences in the cathodic and anodic curves, with a greater effect in the anodic branch.

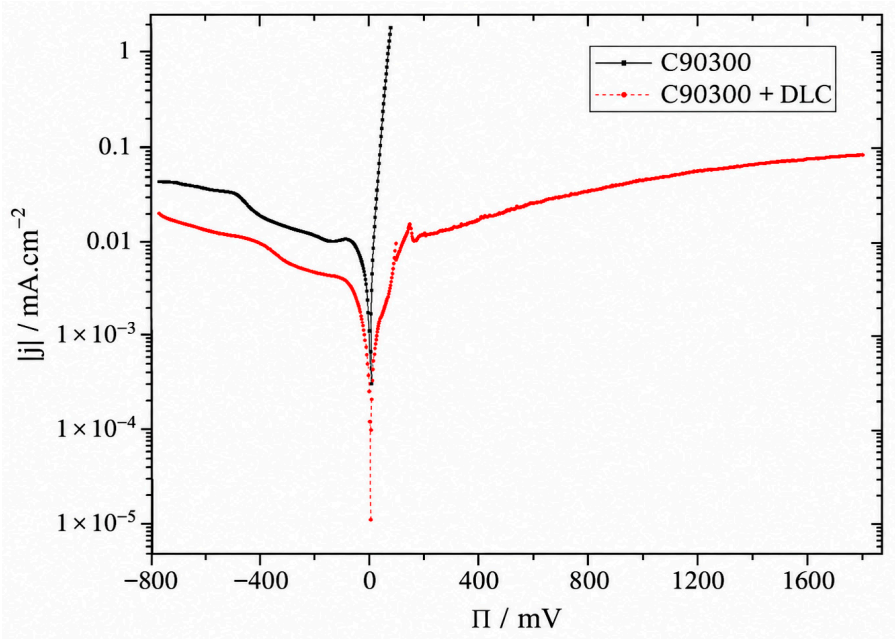


Figure 5. Polarization curves (|j| vs. Π) for (–) uncoated C90300 and (---) C90300/a-Si:H/DLC immersed in a 3.5% NaCl aqueous solution after 1 h.

The corrosion current densities were estimated from the potentiodynamic polarization curves using Tafel extrapolation. This approach assumes that sufficiently linear potential–log (current density) regions can be identified and that the selected branches are predominantly governed by activation-controlled electrochemical kinetics. However, polarization of copper-based alloys in chloride-containing electrolytes may involve oxide-film formation, mass transport, and other processes that can introduce deviations from ideal Tafel behavior. Consequently, the corrosion current densities obtained by extrapolation should be interpreted as approximate values. Figure 6 presents an enlarged view of the polarization curves near the corrosion potential to illustrate the regions considered for analysis.

From these potentiodynamic polarization curves, we determined the corrosion current density (icorr) by extrapolating the linear regions of the anodic and cathodic branches near the corrosion potential (Ecorr). The Tafel analysis yielded cathodic (βc) and anodic (βa) slopes of 75.8 and 49.1 mV dec^{-1} for uncoated C90300 bronze, respectively, whereas the DLC-coated sample exhibited values of 120.0 and 44.1 mV dec^{-1}. The extrapolated corrosion potentials (Ecorr) were −0.2349 V and −0.2090 V, respectively. The uncoated bronze (C90300) exhibited an icorr of approximately 1 × 10^{-2} mA cm^{-2}. Meanwhile, the DLC-coated sample showed a significantly lower value of about 3 x 10^{-4} mA cm^{-2}, indicating a reduced corrosion rate due to the protective effect of the carbon coating. The anodic and cathodic Tafel slopes remained within the expected range for mixed-control

corrosion processes, suggesting that the DLC layer primarily acts as a physical barrier, reducing both the anodic metal dissolution and the cathodic reduction reactions at the interface. An initial protection efficiency (η) of approximately 97% was estimated from the extrapolated corrosion current densities using Equation (2):

$$\eta = 100\% \frac{(j_{corrMetal} - j_{corrDLC})}{j_{corrMetal}} \quad (2)$$

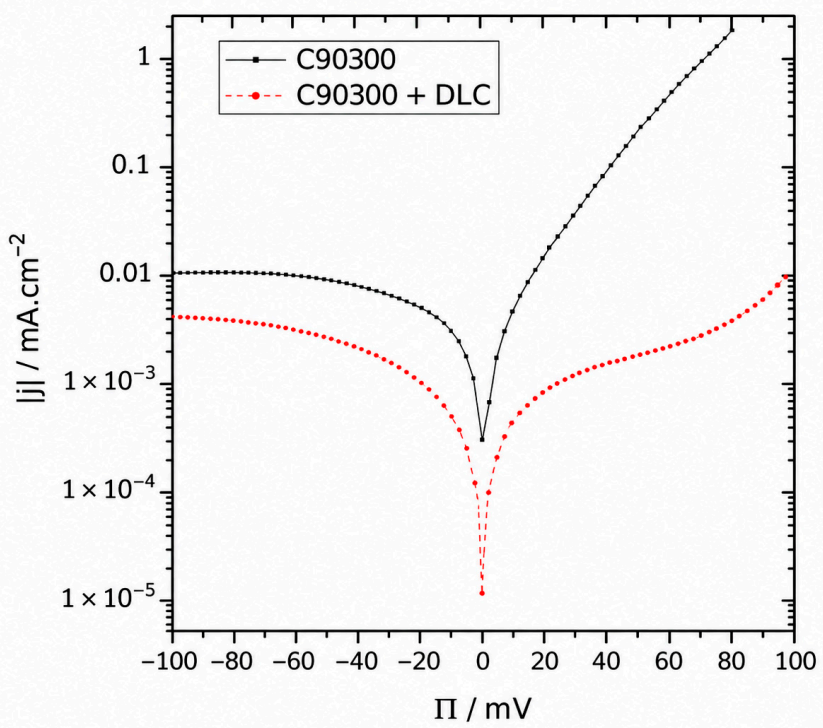


Figure 6. |j| vs. Π for (–) bronze C90300 uncoated and (---) coated E_{corr} ±100 mV.

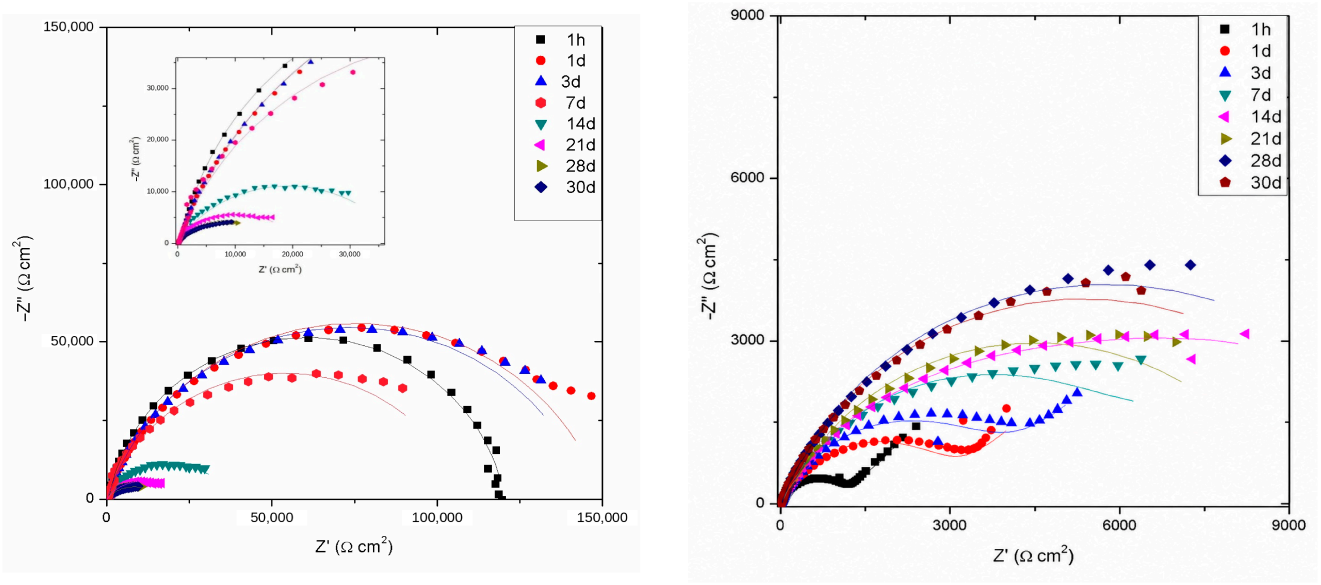
The high initial protection efficiency calculated for the DLC-coated sample is consistent with its distinct electrochemical behavior in both anodic and cathodic polarization regions compared with the uncoated substrate. The lower anodic current densities indicate reduced metal dissolution, consistent with the physical barrier effect of the DLC coating. Similarly, the decrease in cathodic current density demonstrates suppression of cathodic electrochemical activity, which is likely associated predominantly with oxygen reduction under the investigated aerated conditions. This reduction may result from decreased exposure of electrochemically active sites, restricted electrolyte access, and possible limitations in electron transfer through the coating. However, the relative contributions of these mechanisms cannot be independently established from the polarization measurements alone.

3.2.3. Electrochemical Impedance Spectroscopy

To evaluate the time behavior of a DLC film on bronze C90300, we performed EIS measurements at different immersion times up to 30 days in a 3.5% NaCl aqueous solution. The first impedance measurement was taken after 1 h of OCP stabilization at room temperature. The impedance data were collected at 1 h and 1, 3, 7, 14, 21, 28, and 30 days. Figure 7 shows the Nyquist plots, and Figure 8 shows the Bode plots for the EIS experimental response and the fitting model obtained by equivalent electrical circuits.

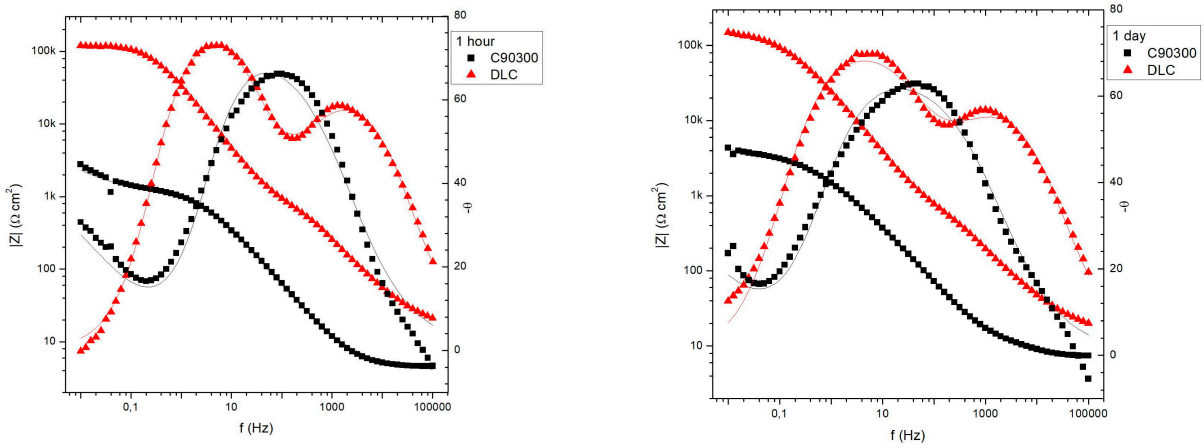
Nyquist plots show a flattened semi-circular shape with capacitive loops across the entire frequency domain for both systems, bronze uncovered and covered with DLC. Such diagrams, with a flattened semi-circular shape, are characteristic of porous layers

and can be related to adsorption pseudo-capacitance [41]. The capacitive loop diameter in the DLC-coated system is larger in every measurement, confirming the anticorrosive protection provided by the DLC film. On the other hand, the capacitive loop diameter for DLC-coated bronze decreased with time, going from $|Z|_{10m\ Hz} \sim 130\ k\Omega.cm^2$ in the first measurement to $|Z|_{10m\ Hz} \sim 10\ k\Omega.cm^2$ after 30 days of immersion, while the capacitive loop for uncoated bronze increased, from $|Z|_{10m\ Hz} \sim 3\ k\Omega.cm^2$ in the first measurement to $|Z|_{10m\ Hz} \sim 8\ k\Omega.cm^2$ after 30 days of immersion. For the C90300/a-Si:H/DLC system, the decrease in the phase angle ($-\theta°$) indicates degradation of the DLC film, while the increase in $-\theta°$ for uncoated bronze indicates the formation of corrosion products that act as a protective coating, increasing impedance. Despite this, over 30 days, the bronze-DLC film Nyquist and Bode phase-angle plot values were higher than those for uncoated bronze.



(**a**) (**b**)

Figure 7. Nyquist impedance plots for uncoated C90300 (**a**) and C90300/a-Si:H/DLC (**b**), immersed in a 3.5% NaCl aqueous solution, along with the simulated curves (solid lines).



(**a**) (**b**)

Figure 8. *Cont.*

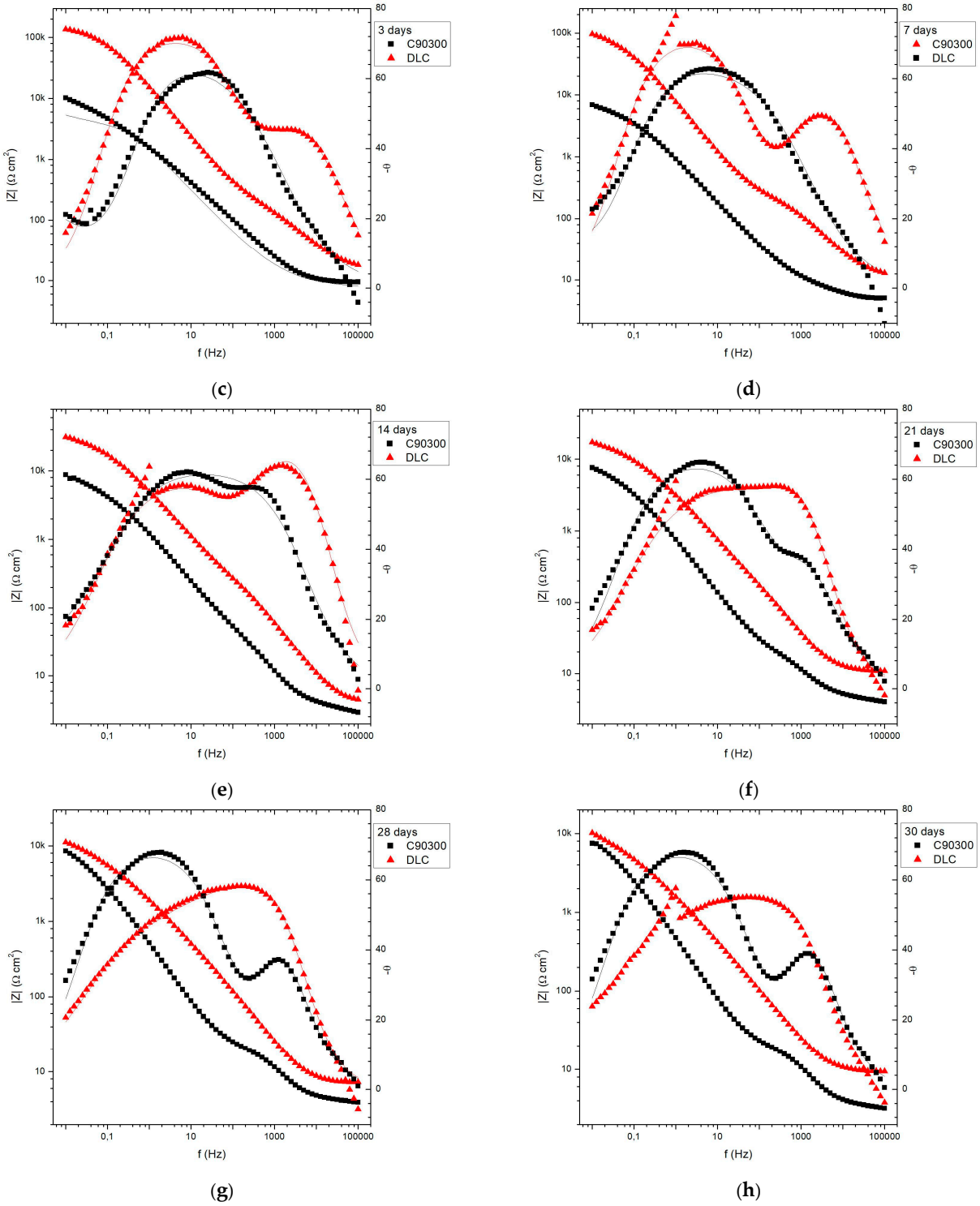


Figure 8. Bode impedance plots for uncoated C90300 (dark square) and C90300/a-Si:H/DLC (red triangle), immersed in a 3.5% NaCl aqueous solution for different days of immersion (**a**) 1 h, (**b**) 1 day, (**c**) 3 days, (**d**) 7 days, (**e**) 14 days, (**f**) 21 days, (**g**) 28 days, and (**h**) 30 days.

The impedance data for uncoated bronze up to day 3 showed a single flattened capacitive loop whose diameter increased with immersion time, associated with one relaxation constant, as confirmed by both the Nyquist and Bode plots (see Figures 7 and 8). In the lower-frequency region, a clear Warburg response, represented by a linear slope close to 45°, indicates diffusion-controlled processes. This diffusional process seems to be masked over time, as shown by the frequency at which the linear profile starts: 0.2 Hz after 1 h and

0.05 Hz after 7 days. After immersion of uncoated bronze for 14 to 30 days, there is just one flattened capacitive loop in the Nyquist plot. In the phase angle Bode plot, this can be associated with two relaxation constants.

Nyquist plots for DLC-coated bronze show a flattened semi-circular shape, a characteristic feature of porous layers or surface roughness. Compared with uncoated bronze, the impedance data differ markedly, with $|Z|_{10m\ Hz} \sim 140\ k\Omega.cm^2$ for C90300/a-Si:H/DLC and $|Z|_{10m\ Hz} \sim 7\ k\Omega.cm^2$ for uncoated bronze after up to 3 days of immersion. These values support DLC's potential to protect bronze against corrosion. For immersion times of 7 days or more, the Nyquist plot profile of bronze-DLC decreased, indicating reduced protective efficacy.

For the Bode plots (Figure 8), the total impedance differs considerably between bronze and bronze-DLC in the first measurement. The difference between the two systems decreased over time, resulting in a slight difference in total impedance after 30 days. This was related to DLC degradation and corrosion product formation and stabilization for bronze-DLC and uncoated bronze, respectively [2,15].

Overall, the DLC-coated bronze exhibited substantially improved initial corrosion resistance, as evidenced by its considerably higher low-frequency impedance compared with the uncoated alloy. However, the progressive decrease in impedance during immersion, from approximately 130 $k\Omega \cdot cm^2$ initially to 10 $k\Omega \cdot cm^2$ after 30 days, indicates partial deterioration of the coating's protective properties. In contrast, the impedance of uncoated bronze increased from approximately 3 to 8 $k\Omega \cdot cm^2$ during the same period, consistent with the formation of corrosion products. Consequently, although the DLC coating maintained a protective effect throughout the investigation, its relative advantage over uncoated bronze diminished substantially after prolonged exposure to the chloride-containing environment.

Following the usual interpretation of the Randles electrical equivalent circuit model, the equivalent electrical circuit consists of a single parallel R-Q circuit. Capacitive loops in a Nyquist plot can be associated with the double-layer capacitance, from which the R-Q circuit can be associated with one relaxation constant [41,42]. As the loops in the Nyquist plots are depressed semicircles, it is preferred to use the constant phase elements (CPEs), represented by the terms Q and n, instead of capacitance (C), to correct the effects of surface roughness and other inhomogeneities or variations in the composition and properties of the surface. The CPE impedance is defined as [2,16]:

$$Z_{CPE} = [Q(i\omega)^n]^{-1} \quad (3)$$

where Q ($\Omega^{-1}.cm^{-2}.s^n$) is the CPE, i ($i^2 = -1$) is the imaginary unit, ω (rad s^{-1}) is the angular frequency, and the exponent n represents the frequency-dispersion feature of the impedance data ($-1 \leq n \leq 1$). The n parameter is a dispersion coefficient associated with uneven current distribution at the electrode surface, resulting in a flattened Nyquist plot due to surface roughness, porous-layer formation, and variations in surface properties or structure [16]. The values of pseudo-capacitances C ($F.cm^{-2}$) associated with each CPE were calculated by the equation:

$$C = \left(R^{1-n}Q\right)^{\left(\frac{1}{n}\right)} \quad (4)$$

where R and Q were taken from the values of the corresponding time constants.

The fitted responses obtained using the equivalent electrical circuit models are superimposed on the experimental Nyquist and Bode plots in Figures 7 and 8. The relative errors reported for the individual fitted circuit parameters were below 10%, while the constant phase element (CPE) exponent (n) ranged from 0.53 to 0.905, indicating deviations from ideal capacitive behavior [2]. The simulated responses reproduce the main features of the

experimental impedance spectra. However, the overall quality of the fitting should be evaluated using quantitative goodness-of-fit statistics, such as reduced chi-square (χ^2) and residual errors, rather than visual agreement alone. Furthermore, agreement between experimental and simulated spectra does not necessarily establish the uniqueness or physical validity of the proposed equivalent circuit models.

Tables 2 and 3 show the simulation results and the circuits for bronze alloy without and with DLC film (Figures 9 and 10), respectively. These simulations used the fitted data from the earlier Nyquist and Bode plots. Figures 9 and 10 show the equivalent circuits simulated for uncoated C90300, bronze alloy without DLC, and C90300/a-Si:H/DLC, respectively.

Table 2. Parameter values calculated for corrosion of uncoated bronze C90300 by non-linear regression of the impedance data using the equivalent electrical circuits in Figure 9.

Circuit	Rp Ωcm^2	n_2	C2 μFcm^{-2}	R2 Ωcm^2	Rw Ωcm^2	n_1	C1 μFcm^{-2}	R1 Ωcm^2	Re Ωcm^2	Time
(A)	982.5				381.1	0.88	53.6	982.5	3.83	1 h
(A)	2777.6				441.38	0.79	90.78	2777.6	6.91	1 d
(A)	3475.2				581.81	0.79	128.44	3475.2	7.62	3 d
(A)	6086.4				297.67	0.76	371.88	6086.4	4.84	7 d
(B)	12,325	0.73	3200	4325		0.7	263.16	8000	2.88	14 d
(C)	9057.7	0.74	512	9050		0.79	26.32	7.7	4.63	21 d
(C)	11,537	0.78	764	11,525		0.86	19	12.33	4.03	28 d
(C)	10,737	0.78	828	10,725		0.86	18.92	12.18	3.3	30 d

Table 3. Parameter values calculated for corrosion of bronze C90300 with a DLC film by non-linear regression of the impedance data using the equivalent electrical circuits from Figure 10.

Circuit	R_p Ωcm^2	n_2	C_2 μFcm^{-2}	R_2 Ωcm^2	n_1	C_1 μFcm^{-2}	R_1 Ωcm^2	R_e Ωcm^2	Time
(A)	1.20×10^5	0.905	5.109	119,680	0.732	1.166	716.8	17.024	1 h
(A)	1.50×10^5	0.817	9.766	149,760	0.695	1.969	376.96	16.512	1 d
(A)	1.46×10^5	0.817	17.344	145,920	0.704	1.373	140.16	14.912	3 d
(A)	1.08×10^5	0.814	38.906	107,520	0.763	1.6875	172.16	11.328	7 d
(B)	3.88×10^4	0.643	72.656	38,528	0.878	2.902	231.04	4.506	14 d
(B)	2.14×10^4	0.586	77.4	21,248	0.861	3.651	152.96	10.816	21 d
(B)	1.73×10^4	0.53	428.125	17,280	0.897	5.75	27.2	7.232	28 d
(B)	1.66×10^4	0.543	584.375	16,576	0.902	5.97	22.72	9.472	30 d

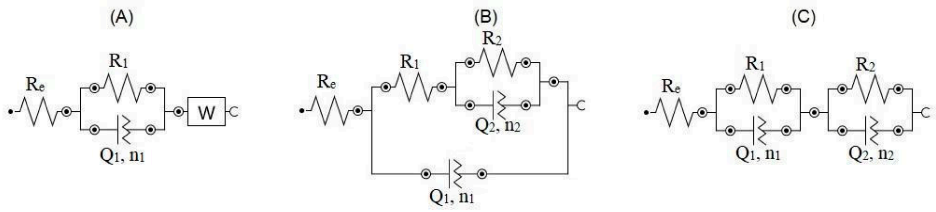


Figure 9. Equivalent electrical circuits used for computer fitting of the experimental results obtained for uncoated bronze C90300: (**A**) equivalent circuit until 7 days; (**B**) equivalent circuit for 14 days; (**C**) equivalent circuit from 21 until 30 days.

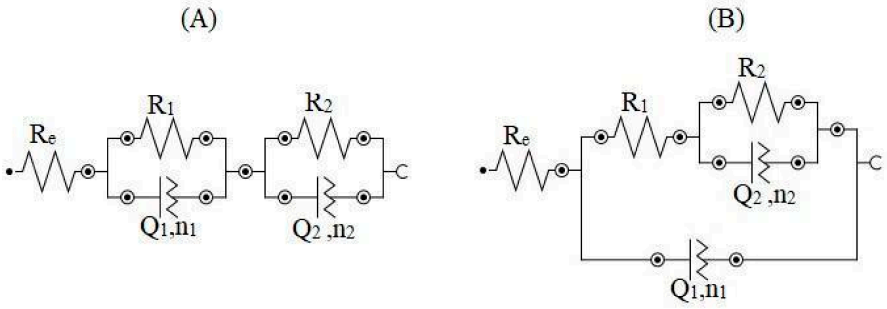


Figure 10. Equivalent electrical circuits used for computer fitting of the experimental results obtained for C90300/a-Si:H/DLC: (**A**) equivalent circuit until 7 days; (**B**) equivalent circuit from 14 until 30 days.

The physical meaning of each circuit element can be interpreted as follows: R_e is the electrolyte resistance between WE and RE; usually, double-layer capacitance and charge transfer are expressed by R_{tc} and C_{dl} to describe charge transfer processes at the electrode/electrolyte interface; the low-frequency elements R_F and C_F are associated with oxidation–reduction processes at the electrode surface, involving surface corrosion products [2,16,29,33,43,44]. When redox reactions take place at a metallic surface, the polarization resistance R_p is better correlated with corrosion resistance than R_{tc}, where R_p is the sum of all faradaic processes and, in this work, can be defined as [2]:

$$R_p \approx R_1 + R_2 \quad (5)$$

For uncoated bronze, the polarization resistance R_p increased up to the 14th day, after which it remained approximately stable. This behavior was related to the development of a corrosion-product film layer that acted as a barrier, increasing total impedance, slowing charge transfer, and reducing the corrosion rate [44]. Otherwise, the increase in corrosion product formation overlapped with the diffusion process over time. Until day 7, R_1 was associated with charge-transfer resistance, and its increase correlated with corrosion product formation. After 14 days, the Nyquist plot presents a flattened arc, and the Bode plot shows two time constants. The increase in C_1 (pseudo-capacitance related to CPE and double-layer capacitance) can be attributed to the formation of a porous, irregular corrosion layer. Impedance data can be related to the redox processes that involve the formation of surface corrosion products by the following reactions [2]:

$$Cu \rightleftharpoons Cu(I)ads + e^- \quad (6)$$

$$Cu(I)ads \rightarrow Cu(II) + e^- \quad (7)$$

Copper ions may precipitate as Cu_2O or CuCl or stay in solution as $[CuCl_2]^-$ and $[CuCl_3]^{2-}$ ions [15]. In a humidified atmosphere, CuCl and $[CuCl_2]^-$ can oxidize to form $Cu_2(OH)_3Cl$:

$$3CuCl + 3/4O_2 + 3/2H_2O \rightarrow Cu_2(OH)_3Cl + CuCl_2 \quad (8)$$

$$3[CuCl_2]^- + 3/4O_2 + 3/2H_2O \rightarrow Cu_2(OH)_3Cl + CuCl_2 + 3Cl^- \quad (9)$$

Tin promotes CuCl and $Cu_2(OH)_3Cl$ production by redox reactions with copper chlorides. Chloride-rich environments produce soluble Sn(II) species and those ions (Sn^{2+} chlorides; $SnCl_2$ and $[SnCl_3]^-$) are strong reducing agents. Consequently, Cu^{2+} ions ($CuCl_2$ and $[CuCl_3]^-$) can be reduced ($[CuCl_2]^-/[CuCl_3]^{2-}$ and/or CuCl), oxidizing tin to SnO_2 [15].

$$SnCl_2 + 2\,CuCl_2 \rightarrow SnCl_4 + 2CuCl \quad (10)$$

$$[SnCl_3]^- + 2[CuCl_3]^- \rightarrow SnCl_4 + 2[CuCl_2]^- + Cl^- \quad (11)$$

$$SnCl_4 + 2\,H_2O \rightarrow SnO_2 + 4\,HCl \quad (12)$$

The formation of high local acidity, due to hydrolysis of copper chlorides and the reaction in Equation (11), can increase Cu ion solubility [15]. In addition, Sn can react with $CuCl_2$ to form $SnCl_2$ and CuCl. CuCl can be oxidized once more, in the presence of water and oxygen, producing $Cu_2(OH)_3Cl$.

$$Sn + 2CuCl_2 \rightarrow SnCl_2 + 2CuCl \quad (13)$$

R_2 increased between 14 and 21 days, then remained nearly stable until 30 days, when C_2 showed high values. These changes may reflect corrosion product growth on the surface, increasing resistance to faradaic processes. In contrast, higher capacitance values were associated with the formation of conductive species (such as SnO_2) [15,45].

Between 21 and 30 days, R_1 values were small compared with earlier times and close to the electrolyte resistance. This behavior is evident in the high-frequency (HF) Nyquist diagram, indicating finite pores in the electrode. Hernández et al. proposed an impedance model for finite pores based on data from studies of pure copper corrosion [40]. Macdonald described the impedance response in Nyquist plots for finite pores, evaluating not only the values but also the shape of the capacitive loop in the HF region [46]. This model explains the low R1 values and confirms the formation of a porous corrosion product. In contrast, the stable R_2 values from 21 to 30 days indicate a relatively stable corrosion product layer on uncoated bronze.

For DLC-coated bronze, Bode plots show two frequency maxima up to 14 days and a flattened arc with a maximum at later measurement times. For this reason, two R-Q circuits were associated with this system. For measurements up to 7 days, we simulated the R-Q pairs in series; for longer times, we simulated them in parallel, with each R-Q product associated with a time constant.

Our findings show that R_1 and R_2 decreased with time (Table 3), indicating DLC degradation. R_2 at 30 days was just 14% of R_2 after 1 h of immersion. Thus, the DLC film acts as a corrosion barrier, and its protective efficacy decreases over time in NaCl medium [47]. The decrease in resistance results from DLC detachment from the bronze surface and chemical changes in DLC composition due to its metastable nature [29,47]. CPE-associated pseudo-capacitance values can corroborate this degradation over time.

The progressive degradation of the DLC coating's protective properties is accompanied by changes in the effective capacitances and CPE exponents obtained from impedance fitting. Both effective capacitances increased overall with immersion time. This behavior may reflect electrolyte penetration, an increased electrochemically accessible area, and additional interfacial and faradaic contributions to the impedance response. The CPE exponents exhibited different trends: n_1 generally increased from 0.732 to 0.902, suggesting a more ideal capacitive response for the first contribution, whereas n_2 decreased from 0.905 to 0.543, indicating a progressively more dispersive response for the second contribution. These changes suggest that different relaxation processes evolve differently during immersion. However, because the equivalent circuit topology changes after 7 days, interpret each fitted element across the entire immersion period with caution. Together with the decrease in polarization resistance, the evolution of the effective capacitances and CPE exponents is consistent with progressive deterioration of the coating's protective performance when immersed in chloride electrolyte.

However, all resistance values are higher and the CPE values are lower for DLC-coated bronze, indicating that DLC provides corrosion resistance for up to 30 days for the tested bronze alloy. Figure 11 shows the time evolution of R_p. For uncoated bronze, R_p increased to a maximum at 14 days and remained almost constant through the end of the experiment (30 days). Bronze coated with DLC showed better corrosion resistance than the bare alloy,

with R_P(DLC) = 122.5 × RP(alloy) after 1 h. At 30 days, the DLC-coated system showed the lowest RP value, but the coated alloy's polarization resistance was still higher than that of the bare alloy (R_P(DLC) = 1.6 × R_P(alloy)).

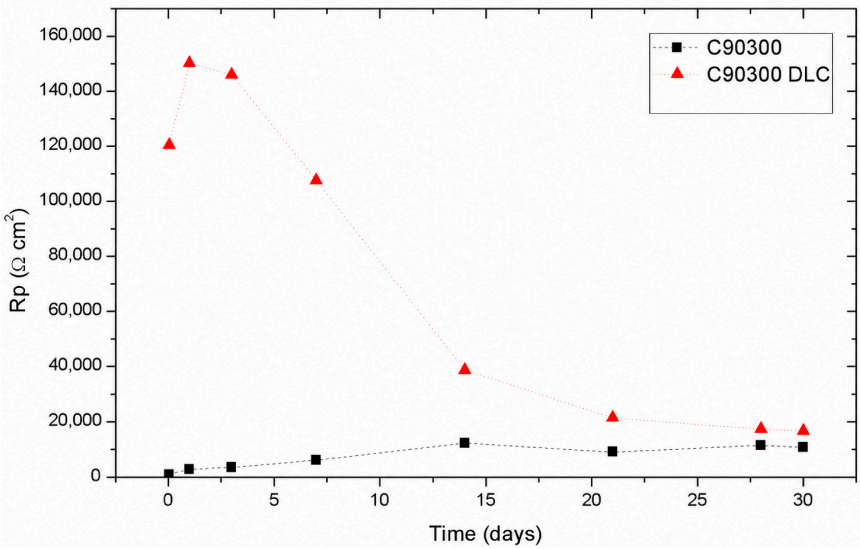


Figure 11. Time evolution of polarization resistance (R_P) for uncoated C90300 (black squares) and C90300/a-Si:H/DLC (red triangles) immersed in a 3.5% NaCl aqueous solution for different days of immersion.

3.2.4. Mott–Schottky Analysis

To investigate DLC-induced inhibition of the cathodic reaction, Mott–Schottky analysis was used to assess the electronic properties of the passive layer and its influence on charge-transfer processes. Since DLC can exhibit semiconducting behavior with limited electronic conductivity, it tends to act as a poor cathode, restricting the kinetics of reduction reactions such as oxygen reduction. Therefore, correlating the Mott–Schottky parameters with the electrochemical results can provide valuable insight into how the DLC layer's electronic structure contributes to its protective effect against corrosion.

Figure 12 shows the graph of $1/C^2$ versus potential, which is related to a typical n-p type junction according to the response of Mott–Schottky analysis. The data indicate the presence of two distinct domains (p-type and n-type), forming an internal heterojunction (p-n), which is common in multilayer coatings, as in this case, and in systems with complex oxides, which Cu_2O/SnO_2 can form.

The general expression above was considered.

$$\frac{1}{C^2} = \frac{2}{q\varepsilon\varepsilon_0 N}\left[E - E_{fb} - \left(\frac{k_B T}{q}\right)\right] \quad (14)$$

C = specific capacitance;

q = elementary charge;

ε = dielectric constant of the material;

ε_0 = vacuum permittivity;

N = charge donor and/or acceptor densities;

The term (k_BT/q) is very small and can be neglected.

Figure 12 presents the Mott–Schottky response ($1/C^2$ versus applied potential) of the DLC-coated bronze. The presence of regions with different slopes suggests distinct apparent semiconducting contributions within the multilayer system. Such behavior may be influenced by the electronic properties of the DLC coating, the a-Si interlayer, and native oxides, including Cu_2O and SnO_2. However, these observations do not indepen-

dently establish the formation of a physical p–n heterojunction, since interfacial states, surface inhomogeneities, and frequency-dependent capacitance may also contribute to the measured response. In the present system, the a-Si interlayer and DLC film may further influence this behavior through their disordered amorphous structures and associated electronic defect states. These defects can introduce localized states that affect charge-carrier transport and trapping. The estimated acceptor-to-donor density ratio ($N_a/N_D \approx 17$; $N_A/N_D = m_D/m_A$; m is the angular coefficient) should therefore be regarded as an apparent parameter derived from the Mott–Schottky model rather than definitive evidence of a physical p–n heterojunction.

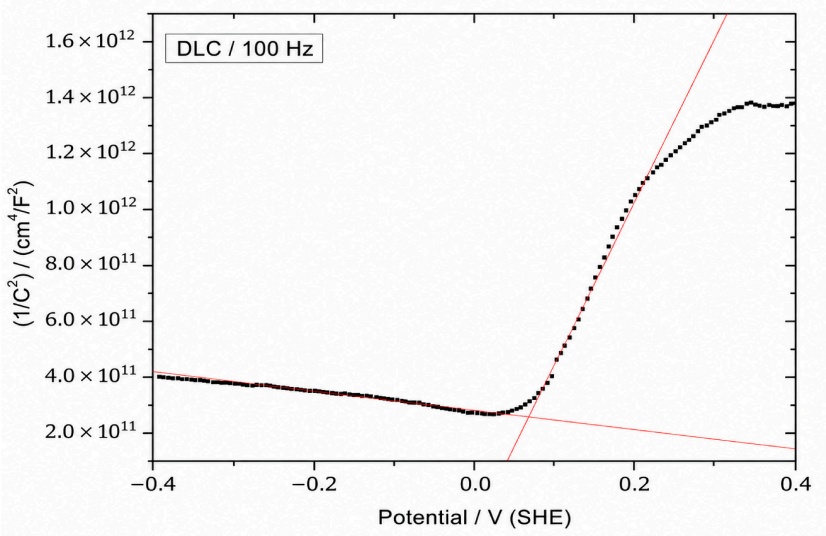


Figure 12. $1/C^2$ versus applied potential (V) for bronze electrode coated by DLC immersed in 0.01 mol L^{-1} $Na_2B_4O_7$ and 0.0125 mol L^{-1} H_3BO_4 solution at 25 °C with applied potential up to −500, −250, 0, +250, and +500 mV (vs. SHE) at 100 Hz (squares represent the experimental data and lines represent linear fits to selected potential regions, highlighting the negative and positive slopes of the capacitance response).

The electronic structure of intrinsic hydrogenated amorphous silicon (a-Si:H) is governed by disorder-induced localized states and band-tail distributions, with the Fermi level typically positioned near the middle of the band gap [48]. The electrical behavior of a-Si:H therefore depends strongly on defects, hydrogen passivation, and doping conditions rather than on intrinsic p- or n-type character. Charge transport in amorphous semiconductors is described as a disorder-mediated process involving localized and partially mobile states [49]. Therefore, the p-n semiconducting response observed in the present DLC/a-Si:H/metallic system likely reflects interfacial effects, defect states, and the electronic contributions of the DLC and metallic phases rather than intrinsic a-Si:H alone.

These distinct semiconducting contributions may generate interfacial potential barriers that hinder electron transport toward the coating–electrolyte interface, potentially contributing to the observed reduction in cathodic oxygen reduction kinetics. Nevertheless, the relative contributions of electronic effects and physical barrier properties cannot be conclusively distinguished from the present measurements. Overall, the Mott–Schottky response suggests the presence of distinct semiconducting contributions within the coated system. However, additional electronic characterization would be required to establish the nature, location, and magnitude of the proposed heterojunction.

The cathodic polarization curves in Figure 13 show that the DLC-coated bronze exhibits substantially lower cathodic current densities than the uncoated C90300 alloy over the investigated potential range. This observation demonstrates a reduction in cathodic

electrochemical activity, consistent with suppression of oxygen reduction under aerated conditions. The Mott–Schottky results suggest that the electronic properties of the multilayer coating may contribute to this behavior by limiting interfacial electron-transfer processes. Nevertheless, the reduced cathodic currents may also arise from the physical barrier effect of the DLC film, including decreased accessibility of electrochemically active sites. Therefore, the present results support a combined protective mechanism involving physical blocking and possible electronic contributions, although their individual effects cannot be quantitatively distinguished. Figure 14 presents the Mott–Schottky response (1/C2 versus applied potential) of the DLC-coated bronze in a different frequency and agrees with previous interpretation.

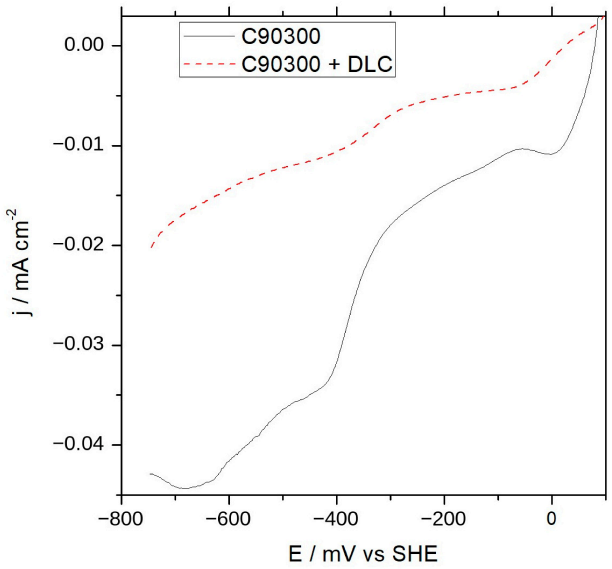


Figure 13. Cathodic polarization curves of (–) bronze C90300 bronze and (---) C90300 bronze coated with DLC in aerated solution. The DLC system shows a significant reduction in cathodic current density, indicating inhibition of reduction reactions and the coating's semiconducting behavior.

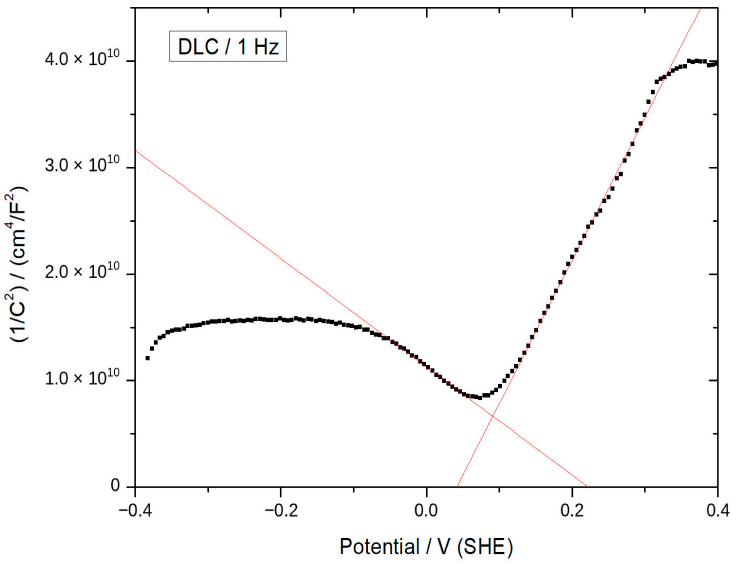


Figure 14. $1/C^2$ versus applied potential (V) for bronze electrode coated by DLC immersed in 0.01 mol L^{-1} $Na_2B_4O_7$ and 0.0125 mol L^{-1} H_3BO_4 solution at 25 °C with applied potential up to −500, −250, 0, +250, and +500 mV (vs SHE) at 1 Hz (squares represent the experimental data and lines represent linear fits to selected potential regions, highlighting the negative and positive slopes of the capacitance response).

3.2.5. Scanning Vibrating Electrode Technique

The SVET map (Figure 15) provides a spatially resolved visualization of the electrochemical processes occurring on the bronze surface, allowing the identification of localized anodic and cathodic sites that drive corrosion. A more diluted NaCl solution (0.01 mol L^{-1}) was used to reduce the electrolyte conductivity, thereby increasing the potential gradients generated by local ionic currents and, consequently, improving their detection by SVET. On a DLC-coated surface, the SVET maps generally show significantly lower current densities and a much more uniform distribution of electrochemical activity. This reflects the DLC layer's effectiveness as a physical and electrochemical barrier that suppresses localized corrosion and stabilizes the surface.

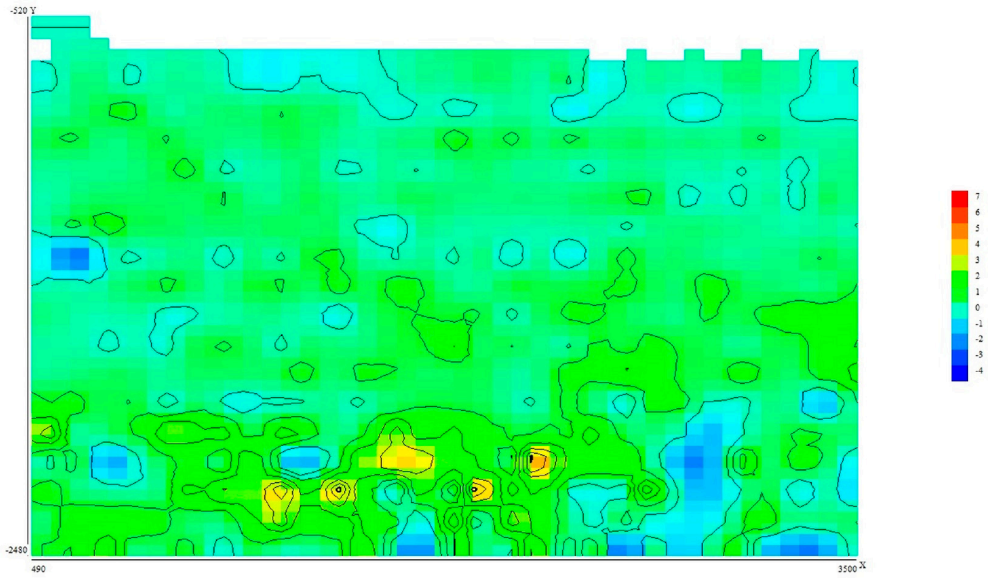


Figure 15. Scanning vibrating electrode technique (SVET) map showing the spatial distribution of local ionic current densities at the surface of DLC-coated C90300 bronze in 0.01 mol L^{-1} NaCl solution.

These SVET observations align with previous results showing that DLC substantially decreases the oxygen reduction reaction and, consequently, the overall cathodic current on the bronze surface. By slowing the cathodic kinetics, the DLC coating reduces the driving force for corrosion, complementing its role as a barrier to anodic dissolution. Together, the SVET and polarization, electrochemical impedance, and Mott–Schottky analysis data provide strong evidence that the C90300/a-Si:H/DLC system mitigates both anodic and cathodic contributions to corrosion, resulting in a more stable and corrosion-resistant bronze surface suitable even for aggressive environments, including maritime applications.

Although we did not perform SVET mapping on uncoated bronze, we established a comparison between coated and uncoated samples independently through polarization and EIS measurements. Consequently, the SVET results are interpreted solely in terms of the DLC-coated system's local electrochemical behavior, without implying a direct quantitative comparison of local current densities between the two surfaces.

3.2.6. Tribological Test

Tribological behavior reveals a pronounced running-in stage followed by a steady-state regime for both materials. Figure 16 shows the coefficient of friction (COF) behavior for both uncoated bronze and DLC-coated bronze. The DLC-coated sample exhibits a lower and more stable COF (~0.50) than the bronze substrate (~0.60–0.65), confirming its lubricating effect. Initially, COF increases due to contact-surface asperities and then stabilizes [50].

Thus, the coating does not degrade the bronze's frictional performance, which is already valued for its relatively low coefficient of friction in engineering applications.

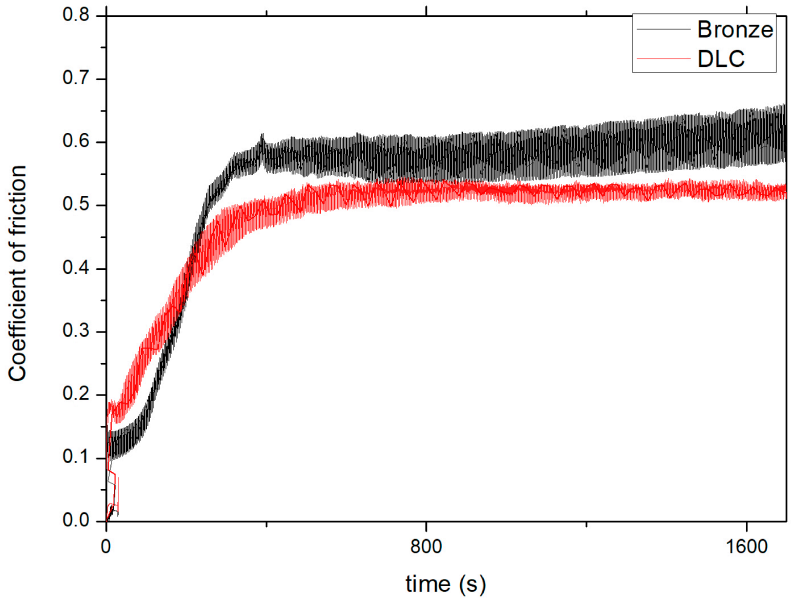


Figure 16. Coefficient of friction as a function of time for the uncoated C90300 Bronze (in black) and the DLC film (in red).

However, this reduction in friction did not reduce wear volume. Profilometric analysis (Figures 17 and 18) revealed a clear transition in wear behavior and distinct morphological differences between the two surfaces. The uncoated bronze (Figure 17) showed a relatively narrow, smooth wear track with limited material displacement. Its maximum measured depth was approximately 0.36 µm, with a cross-sectional area of 66.31 µm^2. This corresponds to an estimated wear volume of 3.32×10^{-4} mm^3 and a specific wear rate of 6.58×10^{-6} mm^3 N^{-1} m^{-1}, indicative of mild adhesive wear with slight plastic deformation.

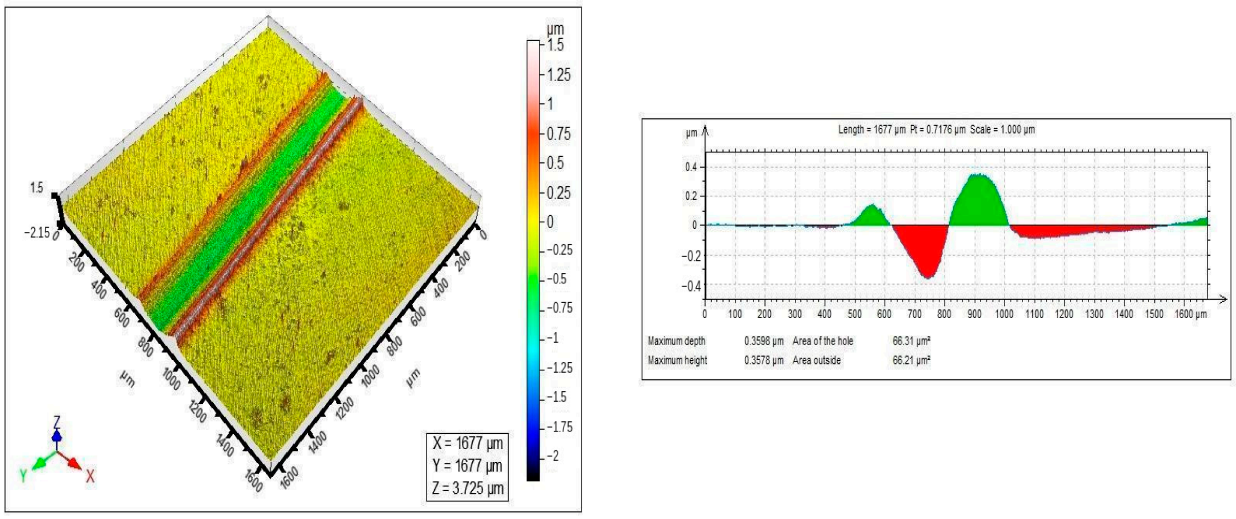


Figure 17. Morphological characteristics and 2D/3D roughness profiles of bronze after the sliding test.

In contrast, the DLC-coated sample (Figure 18) presented a significantly wider, deeper, and more morphologically complex track. The profile showed a maximum depression of ~0.84 µm and an integrated cross-sectional area of 328.1 µm^2. Using the same geometric approach, the estimated wear volume was 1.64×10^{-3} mm^3 (specific wear rate:

3.25×10^{-5} mm^3 N^{-1} m^{-1}), about five times higher than that of the uncoated bronze. This increased severity is supported by the higher post-test surface roughness of the DLC wear track (Sa = 0.5847 µm and Sq = 0.8944 µm) compared to the bronze (Sa = 0.1398 µm and Sq = 0.2655 µm).

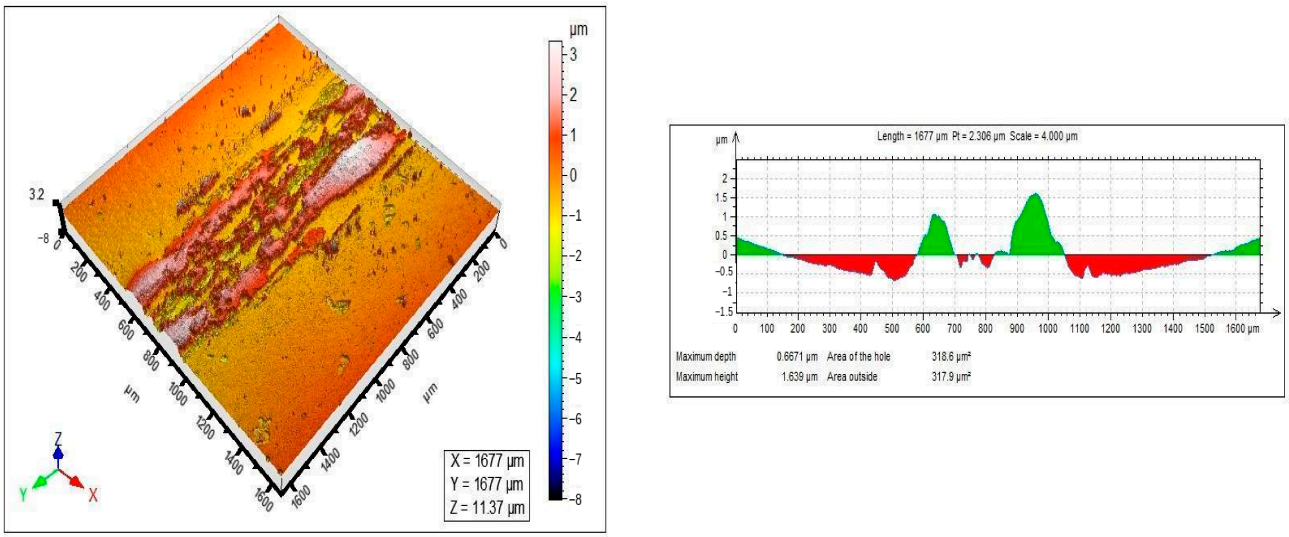


Figure 18. Morphological characteristics and 2D/3D roughness profiles of DLC after the sliding test.

The surface morphology reveals distinct wear behavior between the uncoated bronze and the DLC-coated sample. The uncoated bronze exhibits a relatively narrow and smooth wear track, with limited material displacement, consistent with mild adhesive wear and plastic deformation. In contrast, the DLC-coated surface presents a wider and more irregular wear track, characterized by pronounced depressions and material accumulation along the edges. These features suggest localized coating damage, possible rupture or detachment of the DLC film, and the generation of wear debris during sliding. Limited interfacial adhesion between DLC coatings and metallic substrates may contribute to coating detachment and debris generation [51]; however, adhesion failure cannot be conclusively established without independent adhesion measurements or cross-sectional characterization. The maximum wear-track depth (~0.84 µm) exceeds the measured DLC film thickness (~0.177 µm), suggesting that deformation or material removal may extend beyond the DLC layer into the underlying interlayer and/or bronze substrate. Nevertheless, the measured profile depth alone does not establish the extent of actual substrate wear, since plastic deformation, material displacement, and accumulated debris may also influence the observed topography. Figure 19 shows the contact regions of the steel counterbodies after the tribological tests.

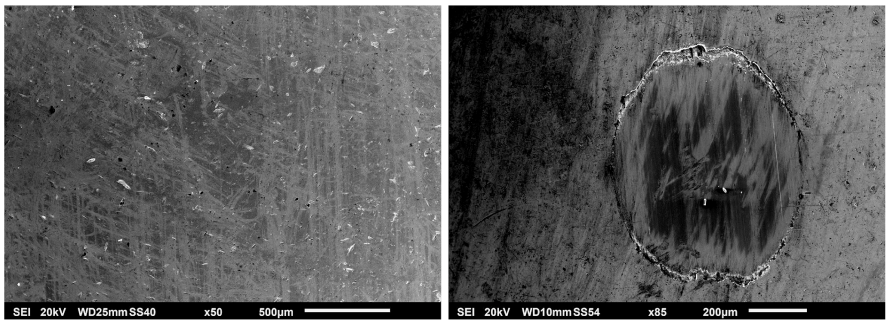


Figure 19. SEM/SE images of the ball after the tribological tests on bronze (**left**) and DLC coating (**right**).

The SEM images of the steel counterbody after the tribological tests (Figure 19) reveal adhered material in the contact region, indicating material transfer during sliding. This transferred material may originate from detached DLC fragments, the underlying substrate, or mechanically displaced wear products. The accumulation of transferred material and wear debris can contribute to the formation of a third-body layer between the contacting surfaces, potentially promoting abrasive interactions and further coating damage. Previous studies have associated DLC wear behavior with structural characteristics involving sp^3-bonded carbon and graphitic regions, which may influence delamination and material transfer processes [52]. However, the present observations do not conclusively establish the origin or composition of the transferred material. Additional compositional analysis of the adhered material and wear debris would be required to distinguish DLC fragments from substrate-derived or counterbody-derived material. Therefore, the observed morphology supports the involvement of material transfer and possible third-body abrasion, while interfacial adhesion failure remains a plausible, but unconfirmed, contributor to the wear process [51,52].

Overall, although the DLC coating reduced and stabilized the coefficient of friction under the investigated conditions, it did not improve the apparent wear resistance of the coated system. The larger wear-track dimensions and greater surface irregularity suggest more extensive mechanical damage than observed for uncoated bronze. These observations are consistent with wear mechanisms involving coating rupture, possible localized delamination, material transfer, and third-body abrasion, as discussed in the literature [51]. However, the estimated wear volume should be interpreted cautiously because the heterogeneous wear-track topography includes depressions, displaced material, and regions of positive height. Consequently, the apparent wear volume calculated from two-dimensional profiles cannot be attributed exclusively to DLC removal or substrate wear. A more accurate determination of material loss would require three-dimensional volumetric analysis relative to the original surface, together with characterization of the wear-track composition and coating integrity. These findings indicate that further optimization of coating adhesion and mechanical durability is necessary to improve tribological performance.

4. Conclusions

The deposition of a diamond-like carbon (DLC) coating using an amorphous hydrogenated silicon (a-Si:H) interlayer substantially improved the initial corrosion resistance of C90300 bronze in a chloride-containing environment. Electrochemical polarization measurements indicated an initial protection efficiency of approximately 97%, while impedance spectroscopy revealed polarization resistance values up to 122 times higher than those of uncoated bronze. The electrochemical results demonstrated a reduction in both anodic and cathodic activity, consistent with the protective barrier effect of the coating. Mott–Schottky analysis suggested the presence of distinct semiconducting contributions within the multilayer system, potentially influencing interfacial electron-transfer processes. However, the precise electronic mechanism responsible for the inhibition of cathodic reactions requires further investigation. Although the DLC-coated bronze maintained higher electrochemical resistance than the uncoated alloy throughout the 30-day immersion period, its protective performance progressively decreased, indicating partial deterioration of the coating under prolonged chloride exposure. Tribological measurements showed that the DLC coating improved frictional stability but did not enhance wear resistance under the investigated conditions. Surface characterization indicated coating damage, material transfer, and possible delamination, highlighting limitations associated with mechanical durability. Overall, the findings demonstrate the potential of DLC/a-Si:H coatings to improve the corrosion resistance of bronze components. Nevertheless, further optimization of coating adhesion,

long-term electrochemical stability, and wear resistance is required before their suitability for demanding applications, including maritime environments, can be established.

Author Contributions: Conceptualization, L.A.d.S., S.M.M.T. and L.F.P.D.; Methodology, L.A.d.S. and L.F.P.D.; Software, L.A.d.S.; Validation, L.A.d.S., S.M.M.T. and V.J.T.-A.; Formal analysis, L.A.d.S., S.M.M.T., V.J.T.-A. and L.F.P.D.; Investigation, L.A.d.S. and L.F.P.D.; Resources, L.A.d.S.; Data curation, L.A.d.S. and L.F.P.D.; Writing – original draft, L.A.d.S., H.S.S. and S.M.M.T.; Writing – review & editing, L.A.d.S., H.S.S. and S.M.M.T.; Visualization, L.A.d.S., S.M.M.T. and L.F.P.D.; Supervision, S.M.M.T. and L.F.P.D.; Project administration, L.A.d.S., H.S.S., S.M.M.T., V.J.T.-A. and L.F.P.D.; Funding acquisition, L.F.P.D., H.S.S. and S.M.M.T. All authors have read and agreed to the published version of the manuscript.

Funding: This study was financed in part by the Coordenação de Aperfeiçoamento de Pessoal de Nível Superior—Brasil (CAPES)—Finance Code 001, with support from CAPES PROEX Química (Pro-cess No. 23038.000341/2019-71) and CAPES Project Nº 42001013016P2 and Nº 42001013056P4. The authors also acknowledge financial support from the Con-selho Nacional de Desenvolvimento Científico e Tecnológico (CNPq), Brazil.

Institutional Review Board Statement: Not applicable.

Informed Consent Statement: Not applicable.

Data Availability Statement: The data presented in this study are available on request from the corresponding author.

Acknowledgments: The authors thank the Microscopy and Microanalysis Center of the Federal University of Rio Grande do Sul (UFRGS) for access to its facilities and the Surface Phenomena Laboratory (LFS) at the Polytechnic School of the University of São Paulo (USP) for providing the facilities used to conduct the tribological experiments.

Conflicts of Interest: The authors declare no conflicts of interest.

References

1. Okayasu, M.; Muranaga, T.; Endo, A. Analysis of microstructural effects on mechanical properties of copper alloys. *J. Sci. Adv. Mater. Devices* **2017**, *2*, 128–139. [CrossRef]
2. Varvara, S.; Caniglia, G.; Izquierdo, J.; Bostan, R.; Găină, L.; Bobis, O.; Souto, R.M. Multiscale electrochemical analysis of the corrosion control of bronze in simulated acid rain by horse-chestnut (*Aesculus hippocastanum* L.) extract as green inhibitor. *Corros. Sci.* **2020**, *165*, 108381. [CrossRef]
3. Li, D.; Franke, P.; Fürtauer, S.; Cupid, D.; Flandorfer, H. The Cu–Sn phase diagram part II: New thermodynamic assessment. *Intermetallics* **2013**, *34*, 148–158. [CrossRef]
4. de Figueiredo Junior, J.C.D.; de Freitas Cunha Lins, V.; De Bellis, V.M. Surface characterization of a corroded bronze-leaded alloy in a salt spray cabinet. *Appl. Surf. Sci.* **2007**, *253*, 7104–7107. [CrossRef]
5. Zohdy, K.M.; Sadawy, M.M.; Ghanem, M. Corrosion behavior of leaded-bronze alloys in sea water. *Mater. Chem. Phys.* **2014**, *147*, 878–883. [CrossRef]
6. Faraldi, F.; Cortese, B.; Caschera, D.; Di Carlo, G.; Riccucci, C.; de Caro, T.; Ingo, G.M. Smart conservation methodology for the preservation of copper-based objects against the hazardous corrosion. *Thin Solid Films* **2017**, *622*, 130–135. [CrossRef]
7. Kareem, K.; Sultan, S.; He, L. Fabrication, microstructure and corrosive behavior of different metallographic tin-leaded bronze alloys part II: Chemical corrosive behavior and patina of tin-leaded bronze alloys. *Mater. Chem. Phys.* **2016**, *169*, 158–172. [CrossRef]
8. Young, M.L.; Schnepp, S.; Casadio, F.; Lins, A.; Meighan, M.; Lambert, J.B.; Dunand, D.C. Matisse to Picasso: A compositional study of modern bronze sculptures. *Anal. Bioanal. Chem.* **2009**, *395*, 171–184. [CrossRef] [PubMed]
9. Silva, C.; Vélez, G.; Colorado, H.A. Patina in the construction of the poetic bronze image: Science of materials, art and philosophy. *Herit. Sci.* **2017**, *5*, 36. [CrossRef]
10. Silva da Conceição, D.K.; Nunes de Almeida, K.; Nhuch, E.; Raucci, M.G.; Santillo, C.; Salzano de Luna, M.; Ambrosio, L.; Lavorgna, M.; Giuliani, C.; Di Carlo, G.; et al. The synergistic effect of an imidazolium salt and benzotriazole on the protection of bronze surfaces with chitosan-based coatings. *Herit. Sci.* **2020**, *8*, 40. [CrossRef]

11. Kestursatya, M.; Kim, J.K.; Rohatgi, P.K. Wear performance of copper–graphite composite and a leaded copper alloy. *Mater. Sci. Eng. A* **2003**, *339*, 150–158. [CrossRef]
12. Wang, Z.; Zhou, R.; Li, Y.; Sun, Y.; Huo, D.; Zhang, H.; Li, Y.; Li, Z. Synergistic enhancement of strength and ductility in leaded nickel-tin bronze by constructing a core-rim dual-phase microstructure via semi-solid squeeze casting. *Mater. Sci. Eng. A* **2025**, *944*, 148902. [CrossRef]
13. Liao, J.; Li, Q.; Zhang, Y.; Ding, Y.; Fan, S.; Liu, Z.; Shen, L.; Tian, Z. High-performance uniform nanocrystalline bronze coatings deposited by friction-assisted jet electrodeposition in deep small blind hole. *Appl. Mater. Today* **2026**, *49*, 103154. [CrossRef]
14. Faraldi, F.; Angelini, E.; Riccucci, C.; Mezzi, A.; Caschera, D.; Grassini, S. Innovative diamond-like carbon coatings for the conservation of bronzes. *Surf. Interface Anal.* **2014**, *46*, 764–770. [CrossRef]
15. Chang, T.; Maltseva, A.; Volovitch, P.; Odnevall Wallinder, I.; Leygraf, C.A. A mechanistic study of stratified patina evolution on Sn-bronze in chloride-rich atmospheres. *Corros. Sci.* **2020**, *166*, 108477. [CrossRef]
16. Wu, J.; Wang, J. The effects of UV and visible light on the corrosion of bronze covered with an oxide film in aqueous solution. *Corros. Sci.* **2019**, *154*, 144–158. [CrossRef]
17. Robbiola, L.; Blengino, J.-M.; Fiaud, C. Morphology and mechanisms of formation of natural patinas on archaeological Cu–Sn alloys. *Corros. Sci.* **1998**, *40*, 2083–2111. [CrossRef]
18. Masi, G.; Esvan, J.; Josse, C.; Chiavari, C.; Bernardi, E.; Martini, C.; Bignozzi, M.C.; Gartner, N.; Kosec, T.; Robbiola, L. Characterization of typical patinas simulating bronze corrosion in outdoor conditions. *Mater. Chem. Phys.* **2017**, *200*, 308–321. [CrossRef]
19. Leygraf, C.; Chang, T.; Herting, G.; Wallinder, I.O. The origin and evolution of copper patina colour. *Corros. Sci.* **2019**, *157*, 337–346. [CrossRef]
20. Di Carlo, G.; Giuliani, C.; Riccucci, C.; Pascucci, M.; Messina, E.; Fierro, G.; Lavorgna, M.; Ingo, G.M. Artificial patina formation onto copper-based alloys: Chloride and sulphate induced corrosion processes. *Appl. Surf. Sci.* **2017**, *421*, 120–127. [CrossRef]
21. Grayburn, R.; Dowsett, M.; Hand, M.; Sabbe, P.-J.; Thompson, P.; Adriaens, A. Tracking the progression of bronze disease—A synchrotron X-ray diffraction study of nantokite hydrolysis. *Corros. Sci.* **2015**, *91*, 220–223. [CrossRef]
22. McCue, I.; Benn, E.; Gaskey, B.; Erlebacher, J. Dealloying and dealloyed materials. *Annu. Rev. Mater. Res.* **2016**, *46*, 263–286. [CrossRef]
23. Sharifi, E.; Ranjbar, K. Dezincification assisted cracking of yellow brass tubes in a heat exchanger. *Eng. Fail. Anal.* **2022**, *136*, 106200. [CrossRef]
24. Song, Z.; Tegus, O. The corrosion properties of bronze alloys in NaCl solutions. *Materials* **2023**, *16*, 5144. [CrossRef] [PubMed]
25. Zhang, L.; Yang, C.; Guo, Y. Corrosion and protection of Chinese bronze relics: A review. *Coatings* **2024**, *14*, 1196. [CrossRef]
26. Bianchi, G.; Longhi, P. Copper in sea-water, potential-pH diagrams. *Corros. Sci.* **1973**, *13*, 853–864. [CrossRef]
27. Oliveira, C.A.G.S.; Stein, M.F.; Saito, E.; Zanin, H.; Vieira, L.S.; Raniero, L.; Trava-Airoldi, V.J.; Lobo, A.O.; Marciano, F.R. Effect of gold oxide incorporation on electrochemical corrosion resistance of diamond-like carbon. *Diam. Relat. Mater.* **2015**, *53*, 40–44. [CrossRef]
28. Robertson, J. Diamond-like amorphous carbon. *Mater. Sci. Eng. R Rep.* **2002**, *37*, 129–281. [CrossRef]
29. Aleixo, L.S.; Ortega, M.R.; Versteg, A.; Falcade, T.; Aguzzoli, C.; Malfatti, C.D.F.; Tamborim, S.M.M. Interfacial effects on anticorrosive and tribological properties of electrodeposited amorphous carbon film on AA2024-T3 aluminum alloys using ethanol as carbon source. *Surf. Interfaces* **2021**, *22*, 100847. [CrossRef]
30. Wei, X.; Yin, P.; Wu, J.; Nie, X.; Lu, Z.; Zhang, G. Deposition of DLC films on the inner wall of U-type pipes by hollow cathode PECVD. *Diam. Relat. Mater.* **2021**, *114*, 108308. [CrossRef]
31. Orazem, M.E.; Frateur, I.; Tribollet, B.; Vivier, V.; Marcelin, S.; Pébère, N.; Bunge, A.L.; White, E.A.; Riemer, D.P.; Musiani, M. Dielectric properties of materials showing constant-phase-element (CPE) impedance response. *J. Electrochem. Soc.* **2013**, *160*, C215–C225. [CrossRef]
32. Capote, G.; Silva, G.F.; Trava-Airoldi, V.J. Effect of hexane precursor diluted with argon on the adherent diamond-like properties of carbon films on steel surfaces. *Thin Solid Films* **2015**, *589*, 286–291. [CrossRef]
33. Manhabosco, T.M.; Martins, L.A.M.; Tamborim, S.M.; Ilha, M.; Vieira, M.Q.; Guma, F.C.R.; Müller, I.L. Cell response and corrosion behavior of electrodeposited diamond-like carbon films on nanostructured titanium. *Corros. Sci.* **2013**, *66*, 169–176. [CrossRef]
34. Danelon, M.R.; de Almeida, L.S.; Manfrinato, M.D.; Rossino, L.S. Study of the influence of a gradient gas flow as an alternative to improve the adhesion of diamond-like carbon film in the wear and corrosion resistance on the nitrided AISI 4340 steel. *Surf. Interfaces* **2023**, *36*, 102352. [CrossRef]
35. Oliveira, M.A.S.; Vieira, A.K.; Massi, M. Electrochemical behavior of the Ti–6Al–4V alloy coated with a-C:H films. *Diam. Relat. Mater.* **2003**, *12*, 2136–2146. [CrossRef]
36. Berretti, E.; Calisi, N.; Capaccioli, A.; Capozzoli, L.; Hamouda, A.M.S.; Giaccherini, A.; Giurlani, W.; Ienco, A.; Martinuzzi, S.; Innocenti, M.; et al. Electrodeposited white bronzes on brass: Corrosion in 3.5% sodium chloride solution. *Corros. Sci.* **2020**, *175*, 108898. [CrossRef]

37. Li, S.; Teague, M.T.; Doll, G.L.; Schindelholz, E.J.; Cong, H. Interfacial corrosion of copper in concentrated chloride solution and the formation of copper hydroxychloride. *Corros. Sci.* **2018**, *141*, 243–254. [CrossRef]
38. Annibaldi, V.; Rooney, A.D.; Breslin, C.B. Corrosion protection of copper using polypyrrole electrosynthesised from a salicylate solution. *Corros. Sci.* **2012**, *59*, 179–185. [CrossRef]
39. Zhang, K.; Lu, J.; Li, J.; Zhang, D.; Gao, L.; Zhou, H. An improved approach to prepare triazole protective film by click-assembly on copper surface. *Corros. Sci.* **2020**, *164*, 108352. [CrossRef]
40. Hernández, R.d.P.B.; Aoki, I.V.; Tribollet, B.; de Melo, H.G. Electrochemical impedance spectroscopy investigation of the electrochemical behaviour of copper coated with artificial patina layers and submitted to wet and dry cycles. *Electrochim. Acta* **2011**, *56*, 2801–2814. [CrossRef]
41. Wolynec, S. *Técnicas Eletroquímicas em Corrosão*; Editora da Universidade de São Paulo (EDUSP): São Paulo, Brazil, 2013. ISBN 9788531407499.
42. Orazem, M.E.; Tribollet, B. *Electrochemical Impedance Spectroscopy*; John Wiley & Sons: Hoboken, NJ, USA, 2008. [CrossRef]
43. Bostan, R.; Varvara, S.; Găină, L.; Petrisor, T.; Mureşan, L.M. Protective effect of inhibitor-containing nitrocellulose lacquer on artificially patinated bronze. *Prog. Org. Coat.* **2017**, *111*, 416–427. [CrossRef]
44. Li, J.; Birbilis, N.; Buchheit, R.G. Electrochemical assessment of interfacial characteristics of intermetallic phases present in aluminium alloy 2024-T3. *Corros. Sci.* **2015**, *101*, 155–164. [CrossRef]
45. Scott, D.A. Bronze disease: A review of some chemical problems and the role of relative humidity. *J. Am. Inst. Conserv.* **1990**, *29*, 193–206. [CrossRef]
46. Macdonald, D.D. Reflections on the history of electrochemical impedance spectroscopy. *Electrochim. Acta* **2006**, *51*, 1376–1388. [CrossRef]
47. Mousavi, S.E.; Naghshehkesh, N.; Amirnejad, M.; Shammakhi, H.; Sonboli, A. Corrosion performance and tribological behavior of diamond-like carbon based coating applied on Ni–Al–bronze alloy. *Trans. Nonferrous Met. Soc. China* **2021**, *31*, 499–511. [CrossRef]
48. Luo, Y.; Flewitt, A.J. Revisiting multiple trapping and release charge transport in amorphous semiconductors exemplified by hydrogenated amorphous silicon. *J. Non-Cryst. Solids* **2025**, *654*, 123436. [CrossRef]
49. Street, R.A. *Hydrogenated Amorphous Silicon*; Cambridge University Press: Cambridge, UK, 1991. [CrossRef]
50. Capote, A.; Capote, G.; Corat, E.J.; Trava-Airoldi, V.J. Effect of low-pressure deposition on the mechanical and tribological properties of a-C:H films deposited via modified pulsed-DC PECVD with active screen as an additional cathode. *Surf. Coat. Technol.* **2022**, *445*, 128716. [CrossRef]
51. Wang, L.; Huang, L.; Wang, Y.; Xie, Z.; Wang, X.F. Duplex DLC coatings fabricated on the inner surface of a tube using plasma immersion ion implantation and deposition. *Diam. Relat. Mater.* **2008**, *17*, 43–47. [CrossRef]
52. Erdemir, A.; Martin, J.-M. Superior wear resistance of diamond and DLC coatings. *Curr. Opin. Solid State Mater. Sci.* **2018**, *22*, 243–254. [CrossRef]

Disclaimer/Publisher's Note: The statements, opinions and data contained in all publications are solely those of the individual author(s) and contributor(s) and not of MDPI and/or the editor(s). MDPI and/or the editor(s) disclaim responsibility for any injury to people or property resulting from any ideas, methods, instructions or products referred to in the content.